

Electron affinity of metal oxide thin films of TiO₂, ZnO and NiO and their applicability in 28.3 THz rectenna devices

S.B. Tekin,^{1,a)} S. Almalki,¹ H. Finch,¹ A. Vezzoli,² L. O'Brien,³ V.R. Dhanak,³ S. Hall,¹ and I.Z. Mitrovic^{1,a)}

¹*Department of Electrical Engineering & Electronics, University of Liverpool, Liverpool L69 3GJ, UK*

²*Department of Chemistry, University of Liverpool, Crown Street, Liverpool, L69 7ZD, UK*

³*Department of Physics and Stephenson Institute for Renewable Energy, University of Liverpool, Liverpool L69 7ZF, UK*

^{a)}Authors to whom correspondence should be addressed. Electronic mail: serdar.tekin@liverpool.ac.uk & ivona@liverpool.ac.uk

Abstract

The holy grail of achieving efficient operation of infrared (IR) rectennas continues to be the realization of a high performance rectifier. In this paper, we have fabricated Metal-Insulator-Metal (MIM) diodes based on TiO₂, ZnO and NiO thin films using shadow mask evaporation, photolithography and sputtering. The electron affinities of oxides have been measured by a combination of variable angle spectroscopic ellipsometry, X-ray photoelectron spectroscopy as well as deduction from the extraction of metal/oxide barrier heights of Fowler-Nordheim tunneling plots. Our results confirm a low value for the electron affinity of NiO_x of ~2.1-2.5 eV which correlates with the high zero-bias dynamic resistance (R_{D0}) of ~500 k Ω of an associated MIM diode. These values render NiO_x to be unsuitable for use in a rectenna device. Better performance has been observed from diodes based on TiO₂ and ZnO_x films. The best rectification performance was achieved for a Au/2.6 nm ZnO_x/Cr diode, scaled down to 1 μm^2 device area, showing a zero-bias dynamic resistance of $R_{D0} = 71$ k Ω , zero-bias responsivity $\beta_0 = 0.28$ A/W and a coupling efficiency $\eta_c = 2.4 \times 10^{-5}$ % for rectification at 28.3 THz. The main significance of this study is that it employs a methodology whereby key parameters of the MIM stack are derived from physical measurements which are then used to assist in the fitting of electrical current voltage data to produce a reliable appraisal of diode performance in an IR rectenna.

Key words: Metal-insulator-metal diodes, electron affinity, X-ray photoelectron spectroscopy, rectification, infrared rectenna.

I. INTRODUCTION

There is a significant demand for the harvesting of renewable infrared (IR) energy from waste heat sources. The mid-IR wavelength range is re-emitted from the earth's surface as radiation with maximum emissivity at $10.6 \mu\text{m}$ (28.3 THz). It is this energy that remains untapped by current solar cell technology. The rectifying antenna (rectenna) device has been shown to be able to capture THz/IR radiation and rectify it into usable direct current (DC) electricity^{1,2}. The Metal-Insulator-Metal (MIM) diode has shown promise for use in IR rectennas. This is due to its ultra-fast, femtosecond range quantum mechanical tunnelling current transport mechanism. The rectification at 28.3 THz has recently been demonstrated by rectenna devices based on MIM diodes using the Au/Al₂O₃/Ti³ configuration. Although the results are promising, the overall conversion efficiency of 2.05×10^{-14} ,³ is low, mainly due to the poor rectification properties of the diodes. Other recent research^{4,5} has focused on the combination of stoichiometric and non-stoichiometric oxides with the aim of engineering the barrier heights to achieve low zero-bias dynamic resistance (R_{D0}) and high zero-bias responsivity (β_0), of vital importance for self-biased rectennas. Khan *et al.*⁶ have reported $R_{D0} = 1.2 \text{ k}\Omega$ and $\beta_0 = 0.125 \text{ A/W}$ for Ti/4 nm ZnO/Pt diode, where the oxide is processed by atomic layer deposition (ALD). However, due to the large active area of $9 \times 10^4 \mu\text{m}^2$, this diode has a very low cut-off frequency defined by $f_c = 1/2\pi R_D C_D$, where R_D and C_D are the diode resistance and capacitance, respectively, and hence low antenna/diode coupling efficiency. It should be noted that for fabricating rectenna arrays to operate at 28.3 THz frequency, the diode area should be much smaller (ideally $\sim 0.01 \mu\text{m}^2$)¹. This is due to the dependency of the f_c on the trade-off between the R_D and C_D . Decreasing the diode area increases the R_D but also decreases the C_D since $C_D = A\epsilon_r\epsilon_0/d$, where d is the thickness of the insulator, ϵ_r is the oxide relative permittivity, ϵ_0 is the permittivity of vacuum and A is the diode area. To achieve a C_D in sub-femtofarad⁵ range, oxides that have low dielectric constant (ϵ_r) and a small diode area (A) is crucial. It is also important to have an ultra-thin film to ensure the dominance of quantum mechanical tunneling. For this reason, it is critical to have low barrier heights in the MIM device structure to achieve a low R_D around zero-bias. To solve this problem, there are several emerging THz rectifier structures such as plasmonic diodes⁷, graphene geometric diodes⁸ and metal-insulator-graphene (MIG) based rectifiers⁹.

The travelling wave diode (TWD) is a particular type of plasmonic rectenna. Pelz *et al.*,⁷ have demonstrated the TWD based on Ni/NiO/Nb₂O₅/CrAu structure that can overcome the impedance limitations of a traditional lumped element of MIM diode. The proposed device involves the excitation of surface plasmon waves in the antenna which are propagated down the extended MIM diode to create a transmission line. The propagating wave is thus rectified by the MIM diode. The TWD showed a peak system responsivity of 130 A/W and a detectivity of $D^* = 1.0 \times 10^4 \text{ Jones (cm}\sqrt{\text{HzW}^{-1}})$.

Another emerging device for THz rectification is the graphene geometric diode, which differs from the MIM variant due to its planar structure and lower capacitance⁸. Since monolayer graphene (G) is a highly conductive material, the reduced resistance of this structure can contribute to an improved impedance match between the antenna and the rectifier. Hence, the associated RC time constant of geometric diodes can be decreased to the femtosecond (10^{-15} s) range, suitable for terahertz rectification^{8,10-13}.

The first graphene-based bowtie antenna-coupled diode that can operate at 28 THz was reported by Zhu *et al.*⁸. The rectenna structure was composed of a 5.1 μm long bowtie antenna with a 500 nm geometric diode at its centre. A diode resistance of ~ 1 k Ω and a zero-bias responsivity of 0.12 AW^{-1} have been achieved. Hemmetter *et al.*,⁹ have demonstrated a one-dimensional (1D) MIG integrated rectenna composed of Ti/TiO₂/G layers on flexible polyimide film. The proposed device was shown to operate up to 170 GHz and exhibited a maximum responsivity of 80 V/W at 167 GHz with a noise equivalent power of 80 pW/ $\sqrt{\text{Hz}}$ in free space measurements under ambient conditions.

Dragoman *et al.*,¹⁰ presented a comprehensive theoretical and experimental study of geometric diodes made from graphene monolayers formed by chemical vapour deposition (CVD) on SiO₂/p-Si wafers. The graphene diode had a shoulder width of 100 nm with a neck width of 20 nm. The cut-off frequency of the device was estimated to be 6.5 THz. In a later study¹¹, it was shown that graphene acts as a reactive impedance surface (RIS), resulting in a more efficient THz antenna. The design of a ballistic diode allows rectification that is controllable by a back-gate voltage. According to the simulations, a direct THz receiver composed of the antenna, matching circuit and diode achieved a responsivity of 21.33 V/W up to 10 THz with a -20 V gate bias and 1 μW input power dissipation. In more recent theoretical work¹², a graphene rectenna was shown to have the potential of achieving a conversion efficiency of 58.43% at 897 GHz using a graphene monolayer on n-doped GaAs.

Araby *et al.*¹³ have investigated various types of graphene-based diodes integrated with antennas for harvesting IR energy. A rhombus-shaped dipole nanoantenna combined with a geometric diode has been proposed for energy harvesting at 19.4 THz using Monte Carlo simulations¹⁴. A transparent transmit-array was proposed to enhance the receiving voltage, achieving a maximum of 97.6 μV with a half-field bandwidth of 10.92 THz. Furthermore, it was reported that the implementation of a Yagi nanoantenna arrangement, with an increased number of directors, increases the received voltage to 39.15 μV . The combination of the transmit-array and Yagi nanoantenna arrangement yielded the best result, with a received voltage of 0.202 mV.

Wang *et al.*,¹⁵ conducted an extensive study of the impact of various graphene-based geometric neck widths on the functionality of the device. A CVD grown monolayer graphene-based geometric diode with β_0 and R_{D0} of 0.0628 A/W and ~ 5 k Ω , respectively for the 50 nm neck width was demonstrated¹⁵, showing potential for THz rectenna applications.”

The main focus of this study, is the investigation of MIM tunnel rectifiers and now present a review of this area. Dodd *et al.*¹⁶ and Kaur *et al.*¹⁷ have demonstrated Ti/TiO_x/Pt and Ti/TiO₂/Pd diodes with $R_{D0} \sim 100$ -200 k Ω and β_0 of 2.25 A/W, however it is difficult to assess the efficiency of these devices due to the lack of published data. The most recent data⁵ show a scaled 0.025 μm^2 Ni/ ~ 1.5 nm NiO/CrAu diode, where the oxide is grown by plasma oxidation, with a much lower $R_{D0} = 630$ Ω in comparison to previously published data on similarly processed NiO-based MIM devices. For example, a similar configuration with a considerably larger area (1.45 μm^2) diode of Ni/3 nm NiO/Cr fabricated by Krishnan *et al.*¹⁸, where the oxide is prepared by plasma oxidation, resulted in a R_{D0} of 500 k Ω . In another similar structure of Ni/NiO/Ni, fabricated by Choi *et al.*¹⁹, with < 4 nm thick plasma oxidized NiO and an aggressively scaled diode area of 0.018 μm^2 , the resulting R_{D0} is in the order of megaohms, i.e. 42.4 M Ω , while β_0 is comparable (= 0.41 A/W) as in Ref. 5. In our latest work²⁰ on the CrAu/NiO/CrAu system, where NiO was processed by radio frequency (RF) sputtering, we also measured a large R_{D0} of 461 k Ω for 1 μm^2 scaled diode area, in line with observed values in Ref. 18, while β_0 was found to be slightly improved to 0.76 A/W. An anomalously low R_{D0} in Ref. 5 has been interpreted to be due to the very small Ni/NiO and CrAu/NiO barriers of 0.1 eV and 0.07 eV respectively. These values were deduced from simulating the theoretical current-voltage (I - V) curve of the MIM stack with assumed band diagram configurations to match the experimental I - V data. This approach is often used in the literature but gives a wide range of values for metal/oxide band diagram parameters that do not agree with values extracted from physical characterization of associated thin films rendering difficulties in interpreting the results. In the case of Ref. 5, the electron affinity (χ) of NiO is deduced to be 4.8 eV from the theoretical I - V curve, while in Ref. 17 using the same fitting approach, χ of a similar plasma oxidized NiO film is estimated to be 2.05 eV. Looking at the published data^{21,22} from ultraviolet and X-ray photoemission spectroscopy (UPS, XPS), the electron affinity of NiO has been measured to be 1.46 eV²¹, while for as-deposited NiO_x, χ is 2.1 eV,²².

Similar variation can be observed in the band gap values of oxide materials, likely to be due to varying stoichiometry and structural properties (crystalline, polycrystalline, amorphous) of films deposited by different methods (plasma oxidation⁵, sputtering²², pulsed laser deposition^{23,24}). For example, the band gap of crystalline NiO was found to be 3.6 eV²³, 3.65 eV²⁴ and 4.0 eV²⁵. On the other hand, the band gap of 2 nm plasma-oxidized NiO films was measured to be 3.4 eV⁵. It has been reported by Ratcliff *et al.*,²² that

the band gap as well as electron affinity of NiO are strongly dependent on the growth method. For example, as-deposited NiO layers exhibited a band gap of 3.1 eV while the Ar ion-sputtered and the O₂ plasma treated NiO layers had values of 0.4 eV and 3.5 eV, respectively²². These studies clearly point to a decrease or increase of electron affinity depending on the surface treatment of NiO, where the band gap structure can also differ.

We present in this paper experimental evidence for the value of the electron affinity of stoichiometric TiO₂, and partially stoichiometric ZnO_x and NiO_x films using a combination of XPS and variable angle electron spectroscopy (VASE) measurements. For NiO_x, we measured χ to be 2.05 eV, in agreement with the work of Ratcliff *et al.*²². The electron affinities deduced from measuring metal/oxide barrier heights (ϕ) from Fowler-Nordheim tunneling (FNT) plots on reference MIM samples were found to agree (± 0.2 eV) with XPS measured χ values for TiO₂ and ZnO_x films. Moreover, we have fabricated MIM diodes based on (< 3 nm) TiO₂ and ZnO thin films to study their suitability for inclusion in 28.3 THz rectennas. The measured electron affinity values were used to fit experimental *I-V* curves of associated MIM diodes. In the light of structures studied in this paper, the best performing diode for inclusion in 28.3 THz rectenna is found to be Au/ZnO_x/Cr with $(R_{D0}, \beta_0) = (71 \text{ k}\Omega, 0.28 \text{ A/W})$ yielding a coupling efficiency of $2.4 \times 10^{-5} \%$.

II. EXPERIMENTAL

The MIM diodes were fabricated on (i) ultra-smooth (0.32 nm rms roughness) 4 cm \times 4 cm Corning glass (CG) using shadow mask evaporation and (ii) on 300 nm SiO₂ on Si substrates using photolithography. The surface roughness of the commercial 300 nm SiO₂/Si substrates was found to vary from 0.53 nm to 0.69 nm over the sample area of 0.48 cm \times 0.48 cm, using the surface mapping analysis tool of the spectroscopic ellipsometer. The fabrication steps using SiO₂/Si substrates are depicted in Figs. 1(a)-(d). Substrates of 300 nm thick SiO₂/Si were used to ensure insulation and uniformity of the bottom electrode contacts. The substrates were initially cleaned in Decon 90 (only CG substrates) with de-ionised water (DIW), acetone, propanol and UV ozone cleaner. The patterning was done using a single layer S1813 positive photoresist, UV exposure and developed using Microposit developer concentrate and then rinsed in DIW. Then, the lift-off was performed after metal deposition using thermal evaporation and followed by oxide deposition by RF sputtering.

A base pressure of $< 1 \times 10^{-6}$ mbar was ensured prior to deposition for both evaporation and sputtering processes to provide high quality thin films. The deposition rate of the thermal evaporation was maintained between 3-4 Å/s to avoid surface roughness and have uniform Al, Au and Cr metal electrodes. ZnO, TiO₂ and NiO films were sputtered using Ar gas with a flow rate of 4-5 sccm and 45 W RF power. RF sputtering

process pressure was kept at $3\text{-}4\times 10^{-3}$ mbar at room temperature. It is noted that the actual thickness of the sputtered thin film layers may vary from the nominal values. One possible reason behind this deviation can be the non-uniformity of the plasma which can affect the sputtering rate of the particles. To mitigate this effect, the same Ar gas flow rate and RF power were applied during each deposition and the deposited films were consistently measured by VASE to optimize the deposition rate. However, the plasma can unintentionally stop during the deposition which requires modification of the gas flow rate and the applied RF power within the same deposition step. Considering that XPS is a surface sensitive characterization technique, the variation in these bulk oxide thicknesses has little effect on the results since these films can be considered as bulk (> 10 nm). On the other hand, for thin films, the nominal 2.5 nm and the actual thicknesses of TiO₂ (2.5 nm) and ZnO (2.6 nm) films were in close agreement with tolerances of ± 0.1 nm. This can be attributed to the lower sputtering time used compared to the time for depositing bulk oxide films. Therefore, better control of the deposition conditions has been maintained without any interruption in the plasma for thin film (< 5 nm) processing. The reference samples of ultra-thin (< 3 nm) TiO₂ and ZnO films on Si were also measured using the mapping tool of the ellipsometer to ensure the uniformity of the insulator films sandwiched between the metal electrodes. The thickness variation over the scan area of 0.48 cm \times 0.48 cm was found to be in the sub-nm range indicating good uniformity of deposited films.

The final layer was fabricated using the same steps as the bottom electrode fabrication. The device areas range from 10^4 μm^2 for devices processed by shadow masking, while photolithography enabled the processing of smaller devices of 4 μm^2 and 1 μm^2 areas. The MIM structures fabricated by photolithography are composed of two overlapping diode arms having 1 μm or 2 μm widths (Figs. 1(e)-(f)), where the oxide film is sandwiched between the overlapping arms, resulting in 1 μm^2 or 4 μm^2 diode areas. The diode arms have a length of 28 μm which enables the fabrication of 1 μm^2 diode areas with a cross-bar structure using photolithography without any misalignment.

Reference samples of deposited oxide films on n-Si(100) were deposited simultaneously in the sputtering chamber to determine thickness, optical properties and electron affinity of the films, using variable angle spectroscopic ellipsometry and X-ray photoelectron spectroscopy techniques. The VASE measurements of reference oxide films were conducted using a J.A. Woollam ellipsometer within a spectral range of $0.7\text{-}5.2$ eV at angles $65\text{-}75^\circ$ in 5° steps. XPS measurements were made using a SPECS monochromated Al $k\text{-}\alpha$ X-ray source ($h\nu = 1486.6$ eV) in an ultra-high vacuum chamber at a base pressure of $\sim 10^{-10}$ mbar. Photoelectron emission spectra were recorded with a PSP Vacuum Technology hemispherical electron energy analyser. The spectrometer was calibrated using the core levels (CLs) and Fermi line of a sputtered silver foil and was operated with an overall resolution of ± 0.1 eV. The electrical performance metrics of the fabricated diodes were analyzed from DC current-voltage measurements. The room temperature $I\text{-}V$

measurements were performed in a dark probe station, using an Agilent B1500 semiconductor parameter analyser.

III. RESULTS AND DISCUSSION

A. THICKNESS AND OPTICAL PROPERTIES OF OXIDE FILMS

Initially, the reference Si wafer was measured to ascertain the thickness of the native oxide which was then used in subsequent fittings of oxide/Si samples. The native oxide thickness was measured as 1.96 nm for the Si substrate under the TiO₂ layer and it was found to be 1.74 nm for the layers under ZnO and NiO. Default TiO₂-Cody Lorentz and ZnO-GenOsc models in the CompleteEase software were used for the TiO₂ and ZnO to fit the experimental (ψ , Δ) versus photon energy data, respectively.

The TiO₂ (CodyLor)²⁶ model has only one Cody Lorentz harmonic oscillator to fit the n and k values of the TiO₂ layer. On the other hand, the ZnO (Gen-Osc)²⁶ model includes three different harmonic oscillators: a parametrized semiconductor oscillator (PSemi) and two Gaussian oscillators. The reason for using these two models is that they give the best fit, that is the lowest mean-squared-error (MSE) values between the experimental and theoretical (fitted) (ψ , Δ) versus photon energy data curves. For the NiO film, since there was no available default model in the CompleteEase software, the modeling was started by fitting the ψ and Δ values of the NiO in the transparent region (0.74 eV – 2.0 eV) using the Cauchy relation. Then, the Cauchy model was parametrized to B-spline²⁶ and fitted for the whole energy range to obtain the n and k characteristics in the full energy spectrum.

Kramers-Kronig consistency between the real and the imaginary part of the dielectric function was preserved in all fittings. The MSE values were found to be 7.7 for TiO₂ (CodyLor), 1.8 for ZnO (GenOsc) and 2.5 for NiO (B-spline) models. The fitted ψ and Δ versus photon energy data for TiO₂, ZnO and NiO are shown in Figs. 2(a)-(c). Figures 2(d)-(f) and Table I show the refractive index (n) and the band gap (E_g) values derived from $(\alpha E)^{0.5}$ versus E or $(\alpha E)^2$ versus E plots, where E is the photon energy and α is the absorption coefficient) for the bulk (>10 nm) oxides. The extracted band gaps of the TiO₂, ZnO and NiO films as well as n @ 632.8 nm (1.96 eV) are consistent with the reported values archived in the CompleteEASE software²⁶ used for the VASE analysis. The thicknesses and the optical constants of the thin oxide films (3 nm nominal) used for the MIM device fabrication were measured using the same method.

B. ELECTRON AFFINITY ESTIMATION OF OXIDE FILMS

The XPS core level peaks were fitted using Voigt functions and a Shirley type background subtraction, performed within the CasaXPS software package. Adventitious carbon C 1s core level binding energy,

calibrated to 284.6 eV, was used to account for any sample charging. Stoichiometry of the metal oxide films was determined by the relative sensitivity factor (RSF) adjusted area ratios of the metal core levels and their corresponding O 1s level. It should be noted that XPS is a surface sensitive technique and the stoichiometry determined here refers to the near to surface composition.

Figure 3(d) shows the Ti 2p_{3/2} peak at 458.76 eV and on the right, the O 1s lineshape for the TiO₂ film. The O 1s CL lineshape is fitted with two components: one for the oxygen in TiO₂ at 530.17 eV and a smaller broad peak at 531.51 eV attributed to adventitious carbon related oxide contamination. The quantitative analysis shows that this film is highly stoichiometric with Ti:O of 0.506:1 corresponding to TiO_{1.98}.

In the case of the ZnO film, Fig. 3(e) shows the Zn 2p_{3/2} peak at 1021.30 eV and on the right, the O 1s lineshape. The O 1s CL lineshape has a main peak due to ZnO at 529.72 eV and a smaller peak at 531.49 eV attributed to adventitious carbon related oxide contamination. The film is found to be approximately stoichiometric with Zn:O of 1.367:1 corresponding to ZnO_{0.73}.

In contrast to the TiO₂ and ZnO films, for the NiO film (Fig. 3(f), left), the XPS lineshape is complicated by the presence of multiple satellite structure. Qualitatively, the Ni 2p_{3/2} CL lineshape corresponds to Ni in the Ni²⁺ state as expected for NiO, with the Ni²⁺ binding energy determined to be 853.68 eV. The lineshape would require multiple fit components which for clarity are not shown in the figure. The O 1s CL spectra (Fig. 3(f), right), show a component from NiO at 529.09 eV and two further broad peaks attributed to carbon contamination. It is noted that the contamination on the NiO films is much greater compared to the other two films. Furthermore, it should be noted that the stoichiometry calculation for NiO is challenging due to the above-mentioned satellite peaks compared to the other two oxides and leads to a higher uncertainty in the result. Although the Ni 2p lineshape qualitatively indicates that the Ni is in the 2⁺ state, Dong *et al.*²⁷ have mentioned that it is difficult to identify the different oxidation states of Ni due to the multiple peaks in the spectrum, and indeed there could be some Ni³⁺ state present as well. Following Mansour *et al.*²⁸, we used the area under the Ni 2p_{3/2} lineshape with the corresponding O 1s peak from the oxide to find the stoichiometry of the film to be about NiO_{0.70}, similar to that found for ZnO and indicating some 3+ oxidation state characteristic. These films are referred to as NiO_x and ZnO_x here.

Figures 3(a)-(c) show the secondary electron cutoff (*SEC*) XPS spectra. The *SEC* measurements were done by first biasing the sample to differentiate the *SEC* values of the sample and the analyser, with the nominal value of applied bias, $V_{app} = -10$ V, and then measuring the *SEC* edge and a reference core level under the same conditions. This reference core level can then be compared to the non-biased core level to precisely determine the energy shift. Once adjusted for the energy shift, the *SEC* value can be determined by linear

intersection of the edge with the spectrum background as depicted in Figs. 3(a)-(c) on the left. Hence, the work function of the oxides, $q\phi$ can be determined as

$$q\phi = hv - (SEC + qV_{app}). \quad (1)$$

Note that Figures 3(a)-(c) on the left depict positions of *SECs* for oxide films where x-axes of BEs were adjusted for V_{app} . The valence band maximum (*VBM*) can be determined in a similar way using valence band spectra, by linear intersection of the VB edge with the spectra background as shown in Figs. 3(a)-(c), right. The extracted parameters of $q\phi$ and *VBM* from XPS spectra shown in Figs. 3(a)-(c) can then be used to determine experimentally the ionization energy (*IE*)

$$IE = q\phi + VBM. \quad (2)$$

The *IE* is found to be (± 0.2 eV) 6.88 eV for TiO₂, 6.71 eV for ZnO_x and 4.80 eV for NiO_x. The electron affinity (χ) can then be calculated using the extracted *IE* and band gap (E_g) from the VASE spectra as²⁹

$$\chi = IE - E_g. \quad (3)$$

Considering the E_g values from Tauc plots shown in Figs. 2(e)-(f), the electron affinity is found to be (± 0.25 eV): 3.56 eV for TiO₂, 3.46 eV for ZnO_x and 2.05 eV for NiO_x. The values correlate with literature values^{22,30,31} within experimental errors, although we note that there are also smaller²¹ and larger³² values reported.

To confirm the electron affinity values measured by XPS, a set of MIM diodes were fabricated using shadow mask evaporation with 3.3 nm TiO₂, 3.0 nm ZnO and 3.9 nm NiO thin oxide films sandwiched between symmetrical Al/Al metal electrodes. During the electrical characterization, the possibility of unintentionally grown native AlO_x layers on the bottom Al electrodes was considered and sufficient bias was applied to achieve the required electric field for the FNT in the oxide of interest according to the static voltage ratio calculations ($V_{ox} = C_{eq}/C_{ox} \times V_{app}$, where V_{ox} is the voltage dropped across the oxide layer, C_{eq} is the equivalent capacitance, C_{ox} is the capacitance of the oxide layer and V_{app} is the applied voltage on the entire MIM structure). The E-fields were found to be between 6.9 MV/cm – 6.3 MV/cm for TiO₂, 6.5 MV/cm – 5.8 MV/cm for ZnO and 6.7 MV/cm – 6.5 MV/cm for NiO layers. Figures 4(a)-(c) show FNT plots for these MIM diodes. A linear relationship between $\ln(J/E^2)$ and $(1/E)$ can be seen, with an $R^2 > 0.999$, which indicates a reliable fit³³ and the dominance of FNT over the bias range. The barrier height at the metal/oxide interface was extracted from the slope of FNT plots ($Slope = -4\sqrt{qm^*}(q\phi)^{3/2}/3q\hbar$), where q is electronic charge, $\hbar = h/2\pi$ is Plank's constant, m^* is oxide effective mass, m_0 is electron mass,

and ϕ - barrier height. Note that there are no consistent data available for the effective mass ratio of thin oxides and values reported in the literature vary between the range of values (0.1-1)^{5,29,33-35} for ultra-thin (<5 nm) films. We have used $m_{eff} = 0.5 \times m_0$ and $0.1 \times m_0$ in fittings in Fig. 4. The extracted barrier heights (ϕ) from Fig. 4 are found to be (± 0.1 eV): 0.62 eV for Al/TiO₂, 0.56 eV for Al/ZnO_x and 1.82 eV for Al/NiO_x. The work function (WF) of Al was measured previously by XPS²⁹ and found to be 4.28 eV. Hence, using $\chi = WF_{Al} - \phi$, the oxide electron affinities deduced from FN barriers shown in Fig. 4 are (± 0.3 eV): 3.66 eV for TiO₂, 3.72 eV for ZnO_x and 2.46 eV for NiO_x.

The physical and electrical characterization data are summarized in Table I. It can be seen that affinity deduced from FNT plots is within the measurement error of ± 0.3 eV with that extracted from a combination of XPS and VASE techniques (termed as χ_{XPS}) for stoichiometric TiO₂ and ZnO_x films. The difference in χ for NiO_x film cannot be explained by a measurement error. The extrapolating the edge of the conduction band, valence band or absorption edge from Tauc plots is within ± 0.3 eV. This deviation is rather intrinsic to the different nature of XPS and FNT methods, where the former is much more surface sensitive as noted above. We have also included the theoretical values of electron affinities derived from charge neutrality level as reported by Robertson³⁶⁻³⁷ for comparison in Table I.

D. RECTIFICATION PERFORMANCE OF TiO₂ AND ZnO_x BASED MIM DIODES

The experimental and theoretically fitted I - V curves of TiO₂ and ZnO_x based MIM devices fabricated by photolithography are shown in Figs. 5(a)-(b) together with extracted rectification parameters of dynamic resistance ($R_D = (dI/dV)^{-1}$) (Fig. 5(c)) and responsivity ($\beta = dI''(V)/2I'(V)$) (Fig. 5(d)). The fitted I - V curves were generated using an in-house simulation model^{38,39}. The model is based on the transfer matrix method (TMM). The current density is calculated using the Tzu-Ezaki equation and subsequent transfer matrix multiplications. The dielectric layer is assumed to consist of multiple slices having different barrier heights by the multi barrier Tzu-Ezaki method. Typically, 50 slices per nanometer is chosen for sufficient simulation accuracy. The best fit to the experimental data in Figs. 5(a)-(b) was achieved by inserting $\chi_{TiO_2} = 3.6$ eV and $\chi_{ZnO_x} = 3.7$ eV, in agreement with values experimentally obtained (see Table I). Other parameters used in simulations are: work functions⁴⁰ of Au and Cr are taken as 5.1 eV and 4.5 eV, respectively; the static dielectric constant of TiO₂ is 25⁴¹ and of ZnO is 9.4⁴², while electron effective mass is $m^* = 0.3m_0$, where m_0 is the free electron mass.

Figures 5 (c)-(d) show the rectification parameters R_{D0} and β_0 of Au/2.5 nm TiO₂/Cr and Au/2.6 nm ZnO/Cr diodes with nominal device area of 4 μm^2 . A smaller dynamic resistance of $R_{D0} = 35$ k Ω can be seen for the ZnO based diode in comparison to 193 k Ω for TiO₂ based device. Even though the zero-bias responsivity

of TiO₂ based diode ($\beta_0=1.2$ A/W) is higher than for the ZnO one ($\beta_0=0.23$ A/W), an order of magnitude lower R_{D0} makes the ZnO_x based diode more advantageous for rectennas due to better diode/antenna coupling efficiency. We further show that scaling the ZnO_x based diode to a size of $1 \mu\text{m}^2$ (see Figs. 5(e)-(f)) can result in $\beta_0=0.28$ A/W and $R_{D0}=71$ k Ω . These diode metrics represent an advance on the previously reported state-of-the-art Ti/ZnO/Pt⁶ device in terms of considerably higher coupling efficiency. The power coupling efficiency (η_c) between the diode and the antenna was calculated by^{3,5,43}

$$\eta_c = 4 \frac{R_A R_D}{(R_A + R_D)^2} / 1 + \left[\omega \frac{R_A R_D}{(R_A + R_D)} C_D \right]^2, \quad (4)$$

where R_A and R_D are antenna and diode resistances, respectively; C_D is the diode capacitance; $\omega = 2\pi f$ is an angular frequency, f is a frequency = 28.3 THz. The antenna reactance is assumed to be negligible compared to that of the diode⁴³. Considering that an antenna has a resistance of $\sim 100 \Omega$ to capture the IR radiation, calculated coupling efficiency (η_c) of our fabricated diodes is summarized in Table II and compared with η_c values reported in the literature. The following high-frequency permittivity values of oxides¹ ($\epsilon_\infty = n^2$, where n is the refractive index) were used for the capacitance calculations: 1.4 for TiO₂,⁴⁴ 2.4 for ZnO,⁴⁵ 3.24 for NiO⁴⁵, all at 28.3 THz. The best performing diode in this work (Au/ZnO_x/Cr with $1 \mu\text{m}^2$ area) has $\eta_c = 2.4 \times 10^{-5} \%$ which is $10^8 \%$ higher than for previously demonstrated Ti/ZnO/Pt⁶ diode with $\eta_c = 4.6 \times 10^{-13} \%$. The Au/TiO₂/Cr has an order of magnitude lower coupling efficiency than the ZnO based one ($\eta_c = 1.6 \times 10^{-6} \%$). According to Table II, the highest $\eta_c = 2.9 \times 10^{-1} \%$ has been reported for Ni/NiO/CrAu⁵ diode that features ~ 1.5 nm oxide thickness and device area of $0.025 \mu\text{m}^2$. The measured R_{D0} for this diode was considerably smaller ($\sim 630 \Omega$) than the other measured values ($500 \text{ k}\Omega$ ^{18,20}, $\sim 40 \text{ M}\Omega$ ¹⁹) on similar diodes. These differing values can be explained by the band alignment structure with the fitted electron affinity of NiO film of 4.8 eV, a considerably higher value than those experimentally measured in the literature^{12,13} and from this work (~ 2 eV). Kaur *et al.*¹⁷ found the barrier height at the Ni/NiO interface to be 0.45 eV by matching the theoretically fitted I - V curve to experimental data. Fitting the I - V curve with $\chi_{\text{NiO}} \sim 2$ eV to the same configuration as in Ref. 5 would result in ~ 6 orders of magnitude higher R_{D0} and projected much lower η_c of $\sim 10^{-6} \%$. A similar uncertainty is also seen in Jayaswal *et al.*³ work. Although the reported η_c is $\sim 1.9 \times 10^{-3} \%$ for the Au/Al₂O₃/Ti diode, as mentioned in Ref. 3, the electron affinity and the work function of the metals deviate significantly from the literature values (± 2 eV) questioning the physical meaning of values extracted from I - V fittings and accuracy of predicted coupling efficiency. Under the evidence of our experimental results, ZnO and TiO₂ based MIM diodes can have a projected $\eta_c > 1\%$. This could be achieved by fabricating thinner insulating layers (~ 1 nm) with a smaller area ($\sim 0.01 \mu\text{m}^2$) and more asymmetric metal configurations such as Au/Ti or Au/Nb instead of Au/Cr to reduce the R_{D0} since Ti (4.1 eV⁴⁶) and Nb (4.1 eV²⁹) metals have smaller work function than Cr (4.5 eV⁴⁰).

In order to confirm this assumption, the I - V characteristics of Au/1 nm TiO₂/Ti and Au/1 nm ZnO/Ti diodes were simulated considering the electron affinity values experimentally measured on reference oxide samples. These simulation results were compared with the experimental I - V curves of the diodes presented in Fig. 6. As can be seen in Figs. 6(a)-(b), there is ~ 2 orders of magnitude increase in the current levels of both TiO₂ and ZnO based diodes with the increased asymmetry due to the difference in Au/Ti metal work functions of 1 eV (work functions of Au and Ti are taken as 5.1 eV⁴⁰ and 4.1 eV⁴⁶), as well as the reduced oxide thickness of 1 nm despite the smaller area (0.01 μm^2) compared to the experimental diodes having 4 μm^2 area. Figs. 6(c) and (d) show the simulated R_{D0} values of Au/1 nm TiO₂/Ti and Au/1 nm ZnO/Ti diodes with an area of 0.01 μm^2 to be 1238 Ω and 783 Ω , respectively.

Considering these values of R_{D0} of the two diodes, the dynamic permittivity of 1.4 for TiO₂ and 2.4 for ZnO (Refs. 1, 31-32) at 28.3 THz and an antenna impedance of 100 Ω , the coupling efficiency, η_c has been calculated and results are shown in Fig. 7. The results suggest that the Au/1 nm TiO₂/Ti and Au/1 nm ZnO/Ti configurations can achieve η_c of 5% and 3% respectively, an order of magnitude improvement in the efficiency to the currently highest reported η_c for the single insulator diodes of $\sim 0.3\%$ (see Table II and Ref. 5). Note that the projected η_c for TiO₂ based diode is higher than for the ZnO based diode due to its lower dynamic permittivity. Figure 7 also includes available experimental data from the literature on the MIM diodes based on the three oxides studied. The fabricated 1 μm^2 ZnO based MIM diode is in advance to the state-of-the-art (Ref. 20) but there is a further modification to this structure (1 nm oxide, 0.01 μm^2 diode area, Au/Ti electrodes) that can be done to compete for inclusion in an infrared rectenna. However, for further increase in the β_0 while keeping a low R_{D0} , double insulator MI²M is crucial. As proposed in the theoretical work of Elsharabasy *et al.*,⁴⁷ the Cr/TiO₂/ZnO/Ti configuration could be a potential candidate to have an efficient rectifier based on their simulated I - V characteristics. However, the electron affinities of TiO₂ and ZnO were considered as 4.20 eV and 4.30 eV in their simulations; 0.6 eV higher than our experimentally derived values for both oxides.

A further confirmation for the validity of these experimental results can be substantiated by the results on double insulator (MI²M) devices. For that purpose, a double insulator Cr/1.8nm TiO₂/4.0 nm ZnO/Cr diode having 10⁴ μm^2 area was fabricated using RF sputtering and shadow mask evaporation processes. Room temperature I - V measurements were performed on the fabricated diodes, the obtained results were compared with the theoretical simulations and included in Fig. 8 (a). The electron affinities of the TiO₂ and ZnO were chosen as 3.60 eV and 3.70 eV based on the experimentally measured values and the work function of Cr was kept as 4.50⁴⁰ eV to preserve the consistency with the single insulator MIM simulations in Fig. 5. The static dielectric permittivity of TiO₂ and ZnO were taken as 25⁴¹ and 9.4⁴² respectively with

an electron effective mass of $m^* = 0.2m_0$, where m_0 is the free electron mass. The ratio of m^* has been changed in the simulations from 0.3 to 0.2 to match with the experimental current magnitude since it is written as the combination of the two oxides in the simulation model. It was observed that the experimental and the theoretical I - V behaviour of the diodes are in close agreement (Fig. 8(a)) which support the electron affinity values found in this work. The resulting R_{D0} , β_0 and maximum η values of this MI²M diode have been found to be 108.8 k Ω (Fig. 8(b)), 1.4 A/W (Fig. 8(c)) and 5.6 at 0.5 V (Fig. 8(d)), respectively from the I - V curve.

Despite the considerably improved η and β_0 , this configuration would result in high metal/oxide barriers and consequently high R_{D0} according to the experimental results. As an alternative, metals having smaller work functions such as Ti or Nb can be combined with these two oxides to fabricate Ti/TiO₂/ZnO/Ti or Nb/TiO₂/ZnO/Nb diodes. Another alternative is changing the growth parameters of the RF sputtered ZnO and TiO₂ layers to modulate the stoichiometry and consequently increase the electron affinity of the oxides such as in Ref. 5; or applying post-deposition treatment such as annealing the thin films at high temperatures. Sharma *et al.*,⁴⁸ reported an increase in the electron affinity of up to 0.5 eV between the spin coated ZnO thin films annealed at 150°C and 250°C. This could be a potential solution for having lower metal/oxide barrier heights. As mentioned in Ref. 5, it is not straightforward to predict the projected η_c of the double insulator configurations without doing an actual optical measurement using a THz source since the high frequency behaviour of the diodes deviate from the DC I - V results more than the single insulator configurations, but the η_c can be experimentally increased >10%,⁴⁷ with the above mentioned proposed solutions. Besides these considerations, together with the variety of supporting values in the literature^{18–22}, our results raise the question regarding the repeatability of a very low barrier of ~0.1 eV between the Ni/NiO interface demonstrated in Ref. 5.

IV. SUMMARY

The bottleneck in achieving a 28.3 THz MIM based rectenna continues to be the limitation resulting from the poorly performing diode leading to low power coupling efficiencies. The significance of this paper is in providing experimentally measured electron affinities of TiO₂, ZnO_x and NiO_x thin films by a combination of spectroscopic ellipsometry, X-ray photoelectron spectroscopy and Fowler-Nordheim I - V plots, with the aim of obtaining reliable parameters of the MIM diode stack to accurately interpret its rectification performance at 28.3 THz. A deviation between electron affinity values determined from secondary electron cut-off spectra and the ones deduced from barriers extracted from electrical characterization has been found to be more apparent for nonstoichiometric oxide films. The best achieved coupling efficiency was found to be $\eta_c = 2.4 \times 10^{-5}\%$ for the Au/2.6 nm ZnO/Cr diode having a device area

of nominal $1 \mu\text{m}^2$ which represents a $10^8\%$ improvement in comparison to the previously demonstrated ZnO based diode. Our calculations provide evidence that the η_c of ZnO and TiO_2 based MIM diodes can be enhanced up to $\sim 5\%$ with further modifications such as reducing the device area to nanometer scale, modifying the growth conditions to increase the electron affinity, reducing the oxide thickness to 1 nm and using metals with lower work functions such as Ti and Nb. These modifications can also be applied in double insulator configurations where the coupling efficiency can be improved beyond 10% which could merit practical application of the rectenna.

Acknowledgement. The authors thank EPSRC, UK, project number EP/K018930/1 and British Council UGC-UKIERI project numbers IND/CONT/G/17-18/18 and F.No.184-1/2018(IC) for funding the work.

Data Availability

The data that support the findings of this study are available from the corresponding author upon reasonable request.

References

- ¹ I.Z. Mitrovic, S. Almalki, S.B. Tekin, N. Sedghi, P.R. Chalker, and S. Hall, *Materials (Basel)*. **14**, 5218 (2021).
- ² A. Nazarov, F. Balestra, V. Kilchytska, and D. Flandre, *Functional Nanomaterials and Devices for Electronics, Sensors and Energy Harvesting* (Springer, 2014).
- ³ G. Jayaswal, A. Belkadi, A. Meredov, B. Pelz, G. Moddel, and A. Shamim, *Mater. Today Energy* **7**, 1 (2018).
- ⁴ D. Matsuura, M. Shimizu, and H. Yugami, *Sci. Rep.* **9**, 1 (2019).
- ⁵ A. Weerakkody, A. Belkadi, and G. Moddel, *ACS Appl. Nano Mater.* **4**, 2470 (2021).
- ⁶ A.A. Khan, G. Jayaswal, F.A. Gahaffar, and A. Shamim, *Microelectron. Eng.* **181**, 34 (2017).
- ⁷ B. Pelz and G. Moddel, *J. Appl. Phys.* **125**, (2019).
- ⁸ Z. Zhu, S. Joshi, S. Grover, and G. Moddel, *J. Phys. D. Appl. Phys.* **46**, 185101 (2013).
- ⁹ A. Hemmetter, X. Yang, Z. Wang, M. Otto, B. Uzlu, M. Andree, U. Pfeiffer, A. Vorobiev, J. Stake, and M.C. Lemme, *ACS Appl. Electron. Mater.* **3**, (2021), 11679.
- ¹⁰ M. Dragoman, A. Dinescu, and D. Dragoman, *Eur. Solid-State Device Res. Conf.* 322 (2013).
- ¹¹ M. Dragoman, M. Aldrigo, A. Dinescu, D. Dragoman, and A. Costanzo, *J. Appl. Phys.* **115**, (2014).
- ¹² M. Dragoman and M. Aldrigo, *Appl. Phys. Lett.* **109**, (2016).
- ¹³ H.A. El-Araby, H.A. Malhat, and S.H. Zainud-Deen, in *2017 34th Natl. Radio Sci. Conf. (IEEE, 2017)*, pp. 15–21.
- ¹⁴ S.H. Zainud-Deen, H.A. Malhat, and H.A. El-Araby, in *2017 Japan-Africa Conf. Electron. Commun. Comput.* (IEEE, 2017), pp. 152–155.
- ¹⁵ H. Wang, G. Jayaswal, G. Deokar, J. Stearns, P.M.F.J. Costa, G. Moddel, and A. Shamim,

Nanomaterials **11**, 1986 (2021).

- ¹⁶ L.E. Dodd, D. Wood, and A.J. Gallant, in *SENSORS, 2011 IEEE* (IEEE, 2011), pp. 176–179.
- ¹⁷ A. Kaur and P. Chahal, *IEEE Access* **6**, 55653 (2018).
- ¹⁸ S. Krishnan, H. La Rosa, E. Stefanakos, S. Bhansali, and K. Buckle, *Sensors Actuators A Phys.* **142**, 40 (2008).
- ¹⁹ K. Choi, F. Yesilkoy, G. Ryu, S.H. Cho, N. Goldsman, M. Dagenais, and M. Peckerar, *IEEE Trans. Electron Devices* **58**, 3519 (2011).
- ²⁰ S.B. Tekin, S. Almalki, A. Vezzoli, L. O'Brien, S. Hall, P.R. Chalker, and I.Z. Mitrovic, *ECS Trans.* **108**, 69 (2022).
- ²¹ H. Wu and L.-S. Wang, *J. Chem. Phys.* **107**, 16 (1997).
- ²² E.L. Ratcliff, J. Meyer, K.X. Steirer, A. Garcia, J.J. Berry, D.S. Ginley, D.C. Olson, A. Kahn, and N.R. Armstrong, *Chem. Mater.* **23**, 4988 (2011).
- ²³ J.Y. Zhang, W.W. Li, R.L.Z. Hoye, J.L. MacManus-Driscoll, M. Budde, O. Bierwagen, L. Wang, Y. Du, M.J. Wahila, and L.F.J. Piper, *J. Mater. Chem. C* **6**, 2275 (2018).
- ²⁴ J. Zhang, S. Han, M. Cui, X. Xu, W. Li, H. Xu, C. Jin, M. Gu, L. Chen, and K.H.L. Zhang, *ACS Appl. Electron. Mater.* **2**, 456 (2020).
- ²⁵ E.Z. Kurmaev, R.G. Wilks, A. Moewes, L.D. Finkelstein, S.N. Shamin, and J. Kuneš, *Phys. Rev. B* **77**, 165127 (2008).
- ²⁶ J.A. Woollam, JA Woollam Co. Inc, New England. United States Am. (2011).
- ²⁷ M.D. Dong, J.Y. Shen, C.Y. Hong, P.X. Ran, R.-H. He, H.W. Chen, Q.Y. Lu, and J. Wu, *J. Appl. Phys.* **132**, 173901 (2022).
- ²⁸ A.N. Mansour, *Surf. Sci. Spectra* **3**, 231 (1994).
- ²⁹ I.Z. Mitrovic, A.D. Weerakkody, N. Sedghi, J.F. Ralph, S. Hall, V.R. Dhanak, Z. Luo, and S. Beeby, *Appl. Phys. Lett.* **112**, 3 (2018).
- ³⁰ S.A. Chambers and P. V Sushko, *Phys. Rev. Mater.* **3**, 125803 (2019).
- ³¹ M.C. Gwinner, Y. Vaynzof, K.K. Banger, P.K.H. Ho, R.H. Friend, and H. Sirringhaus, *Adv. Funct. Mater.* **20**, 3457 (2010).
- ³² Z. Liu, Y. Liu, X. Wang, W. Li, Y. Zhi, X. Wang, P. Li, and W. Tang, *J. Appl. Phys.* **126**, 45707 (2019).
- ³³ N. Alimardani, S.W. King, B.L. French, C. Tan, B.P. Lampert, and J.F. Conley, *J. Appl. Phys.* **116**, (2014).
- ³⁴ E.W. Cowell III, N. Alimardani, C.C. Knutson, J.F. Conley Jr, D.A. Keszler, B.J. Gibbons, and J.F. Wager, *Adv. Mater.* **23**, 74 (2011).
- ³⁵ S. Grover and G. Model, *IEEE J. Photovoltaics* **1**, 78 (2011).
- ³⁶ J. Robertson, *J. Vac. Sci. Technol. A Vacuum, Surfaces, Film.* **31**, 050821 (2013).
- ³⁷ J. Robertson, *J. Vac. Sci. Technol. B Microelectron. Nanom. Struct.* **18**, 1785 (2000).
- ³⁸ N. Sedghi, J.F. Ralph, I.Z. Mitrovic, P.R. Chalker, and S. Hall, *Appl. Phys. Lett.* **102**, 92103 (2013).
- ³⁹ N. Sedghi, J.W. Zhang, J.F. Ralph, Y. Huang, I.Z. Mitrovic, and S. Hall, in *2013 Proc. Eur. Solid-State Device Res. Conf.* (IEEE, 2013), pp. 131–134.

This is the author's peer reviewed, accepted manuscript. However, the online version of record will be different from this version once it has been copyedited and typeset.
PLEASE CITE THIS ARTICLE AS DOI: 10.1063/5.0157726

- ⁴⁰ H.B. Michaelson, J. Appl. Phys. **48**, 4729 (1977).
- ⁴¹ Q. Cui, M. Sakhdari, B. Chamlagain, H.-J. Chuang, Y. Liu, M.M.-C. Cheng, Z. Zhou, and P.-Y. Chen, ACS Appl. Mater. Interfaces **8**, 34552 (2016).
- ⁴² N.H. Langton and D. Matthews, Br. J. Appl. Phys. **9**, 453 (1958).
- ⁴³ A. Belkadi, A. Weerakkody, and G. Moddel, Nat. Commun. **12**, 1 (2021).
- ⁴⁴ J. Kischkat, S. Peters, B. Gruska, M. Semtsiv, M. Chashnikova, M. Klinkmüller, O. Fedosenko, S. MacHulik, A. Aleksandrova, G. Monastyrskiy, Y. Flores, and W.T. Masselink, Appl. Opt. **51**, 6789 (2012).
- ⁴⁵ M.R. Querry, *Optical Constants* (Missouri Univ-Kansas City, 1985).
- ⁴⁶ W.F. Gale and T.C. Totemeier, *Smithells Metals Reference Book* (Elsevier, 2003).
- ⁴⁷ A.Y. Elsharabasy, M.H. Bakr, and M.J. Deen, Results Mater. **11**, 100204 (2021).
- ⁴⁸ A. Sharma, S.E. Watkins, G. Andersson, and D.A. Lewis, Energy Technol. **2**, 462 (2014).

Table Captions

TABLE I. The experimentally determined electron affinities from XPS/VASE and FNT measurements of TiO_2 , ZnO_x and NiO_x films are summarized together with reference values from the literature. The thickness (t_{ox}), refractive index (n) and band gap (E_g) values are derived from VASE measurements. The XPS extracted parameters include key core level binding energies (BEs), stoichiometry, ionization energy (IE) and valence band maximum (VBM) of oxide films. The barrier heights (ϕ) between Al/oxide are listed as obtained from FNT plots shown in Fig. 4. Refs. 21, 22, 29-31 refer to experimental XPS/IPES/UPS measured values while Refs. 36, 37 are from theoretical calculations.

TABLE II. A summary of MIM diode rectification figures of merit (R_{DO} , β_0) of devices fabricated based on TiO_2 , ZnO and NiO films and their comparison with the state-of-the-art. The stated coupling efficiency (η_c) values refer to a frequency of 28.3 THz.

Figure Captions

FIG. 1. The fabrication process flow for patterning the MIM rectifiers including (a) substrate cleaning, (b) bottom electrode patterning and deposition, (c) oxide deposition, (d) top electrode patterning and deposition, (e) computer-aided design (CAD) of the photomask showing circular metal electrode patches and the overlapping diode arms, (f) zoomed-in image of the overlapping diode arms showing its length of $28\ \mu\text{m}$ and width of $1\ \mu\text{m}$ or $2\ \mu\text{m}$ used for processing diode area of $1\ \mu\text{m}^2$ or $4\ \mu\text{m}^2$.

FIG. 2. The experimental ψ (amplitude ratio) and Δ (phase difference) parameters measured at 65° , 70° and 75° angle of incidences fitted with theoretical models for (a) TiO_2 , (b) ZnO and (c) NiO . Refractive index (n) and $(\alpha E)^{0.5}$ or $(\alpha E)^2$ versus photon energy (E) plots, where α is absorption coefficient for: (d) TiO_2 , (e) ZnO and (f) NiO films on Si substrates. The band gap (E_g) of each oxide was calculated from the linear extrapolation of the plots to the base line, as depicted.

FIG. 3. X-ray photoelectron intensity spectra of secondary electron cutoff and valence band edge (a-c), and metal and O 1s core level spectra (d-f) for TiO_2 , ZnO and NiO films. The Ni 2p lineshape is complicated due to the presence of satellite structure and for clarity the fitting components are not shown. The x-axis in (a)-(c) left is adjusted for applied bias as stated in Eq. (1).

FIG. 4. Experimental and fitted Fowler-Nordheim plots for (a) TiO_2 , (b) ZnO and (c) NiO based MIM diodes with Al/Al metal electrodes. The values of metal/oxide barrier heights extracted from linear fitting are stated in the insets of each figure.

FIG. 5. Experimental and fitted I - V characteristics of (a) $\text{Au}/\text{TiO}_2/\text{Cr}$, (b) $\text{Au}/\text{ZnO}/\text{Cr}$ diodes with $4\ \mu\text{m}^2$ device area and their (c) dynamic resistance vs. applied bias; (d) responsivity vs. applied bias curves. (e) Experimental and fitted I - V characteristics of scaled $\text{Au}/\text{ZnO}/\text{Cr}$ diode with a nominal device area of $1\ \mu\text{m}^2$ with associated (f) dynamic resistance and responsivity vs. bias curves. The zero bias dynamic resistance (R_{D0}) and zero-bias responsivity (β_0) are stated for each device.

FIG. 6. Comparison between the experimental and simulated I - V curves of (a) TiO_2 and (b) ZnO based single insulator diodes and (c)-(d) their calculated dynamic resistance.

FIG. 7. A summary of experimental and projected η_c for TiO_2 , ZnO and NiO based single insulator diodes.

FIG. 8. Experimental and simulated (a) I - V characteristics $\text{Cr}/2\ \text{nm}\ \text{TiO}_2/4\ \text{nm}\ \text{ZnO}/\text{Cr}$ diode with a device area of $10^4\ \mu\text{m}^2$ with associated (b) dynamic resistance, (c) responsivity and (d) asymmetry curves.

This is the author's peer reviewed, accepted manuscript. However, the online version of record will be different from this version once it has been copyedited and typeset.
PLEASE CITE THIS ARTICLE AS DOI: 10.1063/1.50157726

TABLE I.

Measurement method	Extracted parameters	TiO ₂		ZnO _x		NiO _x	
		Ti 2p _{3/2}	O 1s	Zn 2p _{3/2}	O 1s	Ni 2p _{3/2}	O 1s
	<i>BE</i> (± 0.1) (eV)	458.8	530.2	1021.3	529.7	853.7	529.1
XPS	Metal:Oxygen Stoichiometry	0.506:1 TiO _{1.98}		1.367:1 ZnO _{0.73}		1.425:1 NiO _{0.70}	
	<i>IE</i> (± 0.2) (eV)	6.88		6.71		4.80	
	<i>VBM</i> (± 0.2) (eV)	2.82		2.13		0.21	
	χ_{XPS} (± 0.25) (eV)	3.56		3.46		2.05	
	VASE	<i>t_{ox}</i> (± 0.1) (nm)	24.0		36.2		30.5
<i>n</i> @ 1.96 (eV)		2.13		1.84		1.87	
<i>E_g</i> (± 0.1) (eV)		3.32		3.25		2.75	
FNT	$\phi_{\text{Al/oxide}}$ (eV)	0.62		0.56		1.82	
	χ (± 0.3) (eV)	3.66		3.72		2.46	
Reference	χ (eV)	3.9 ^{30,36,37}		3.6 ³¹ , 4.3-4.5 ³² , 4.6 ³⁶		1.46 ²¹ , 2.1 ²² , 3.0 ³⁶	

This is the author's peer reviewed, accepted manuscript. However, the online version of record will be different from this version once it has been copyedited and typeset.
PLEASE CITE THIS ARTICLE AS DOI: 10.1063/1.50157726

TABLE II.

MIM diode structure	Oxide deposition method	t_{ox} (nm)	Area (μm^2)	β_0 (A/W)	R_{D0} (Ω)	η_c (%)
Au/Al ₂ O ₃ /Ti ³	ALD	1.5	0.04 [†]	0.44	98 k	1.9×10 ^{-3*}
Ni/NiO/Ni ¹⁹	Plasma oxidation	<4.0	0.018	-0.41	42 M	1.5×10 ^{-4 *}
Ni/NiO/Cr ¹⁸	Plasma oxidation	~2.5	1.45	0.50	500 k	1.3×10 ^{-6 *}
Ni/NiO/CrAu ⁵	Plasma oxidation	1.5	0.025	0.41	630	2.9×10 ⁻¹
CrAu/NiO/CrAu ²⁰	RF Sputtering	6.8	~1	0.76	461 k	1.5×10 ⁻⁵
Ti/TiO _x /Pt ¹⁶	Self-oxidation	-	150	2.25	170 k	--
Ti/TiO ₂ /Pd ¹⁷	in-situ oxidation	3	--	--	100 k	--
Au/TiO _x /Cr (this work)	RF Sputtering	2.5	~4	1.2	193 k	1.6×10 ⁻⁶
Ti/ZnO/Pt ⁶	ALD	4.0	9×10 ⁴	0.125	1.2k	4.6×10 ^{-13 *}
Au/ZnO _x /Cr (this work)	RF Sputtering	2.6	4	0.23	35 k	3.3×10 ⁻⁶
Au/ZnO _x /Cr (this work)	RF Sputtering	2.6	~1	0.28	71 k	2.4×10 ⁻⁵

* Coupling efficiency calculated based on the stated thickness, area and R_D values.

[†] Device area calculated based on stated dimensions.

• Oxidation in an elevated temperature and humidity.

This is the author's peer reviewed, accepted manuscript. However, the online version of record will be different from this version once it has been copyedited and typeset.
PLEASE CITE THIS ARTICLE AS DOI: 10.1063/5.0157726

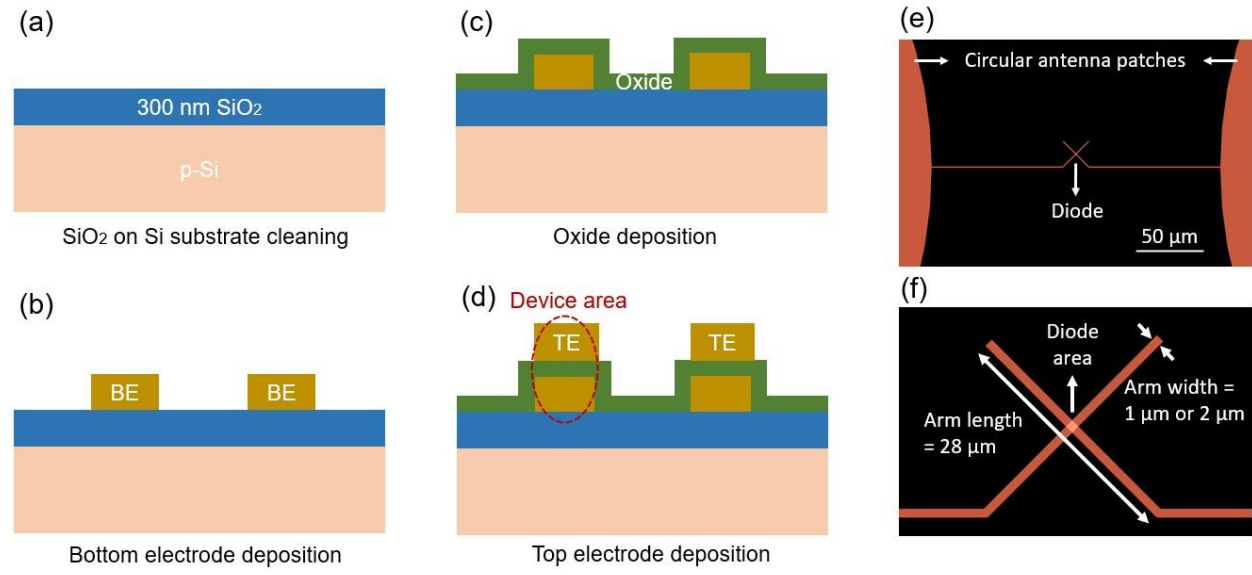


FIG. 1.

This is the author's peer reviewed, accepted manuscript. However, the online version of record will be different from this version once it has been copyedited and typeset.
PLEASE CITE THIS ARTICLE AS DOI: 10.1063/5.0157726

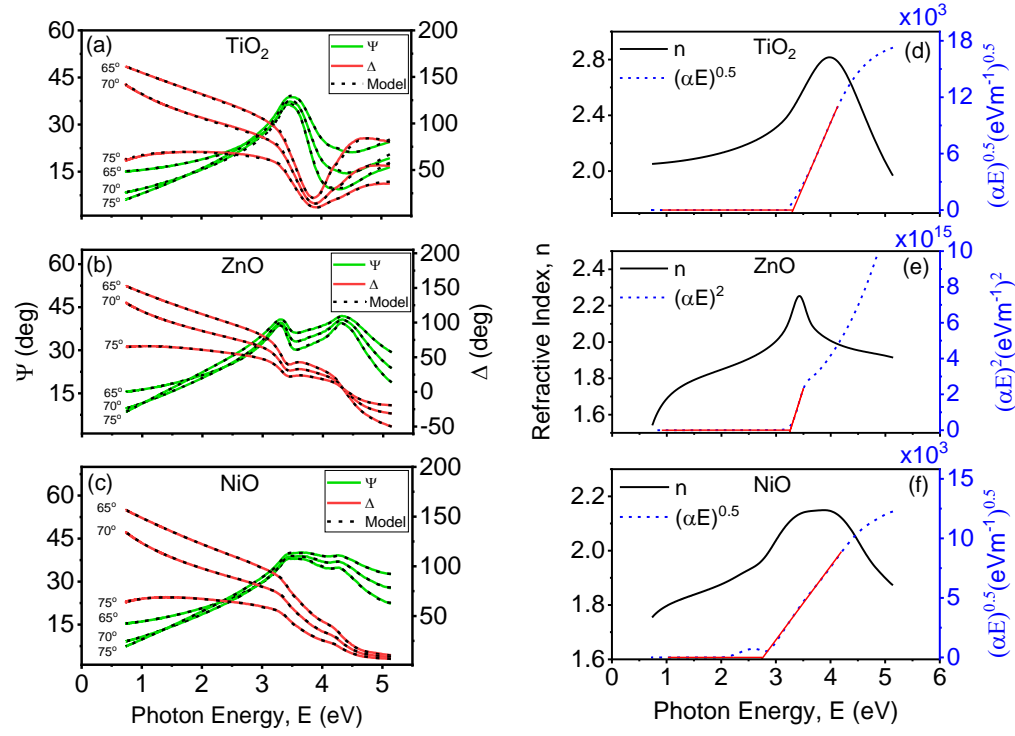


FIG. 2.

This is the author's peer reviewed, accepted manuscript. However, the online version of record will be different from this version once it has been copyedited and typeset.
PLEASE CITE THIS ARTICLE AS DOI: 10.1063/5.0157726

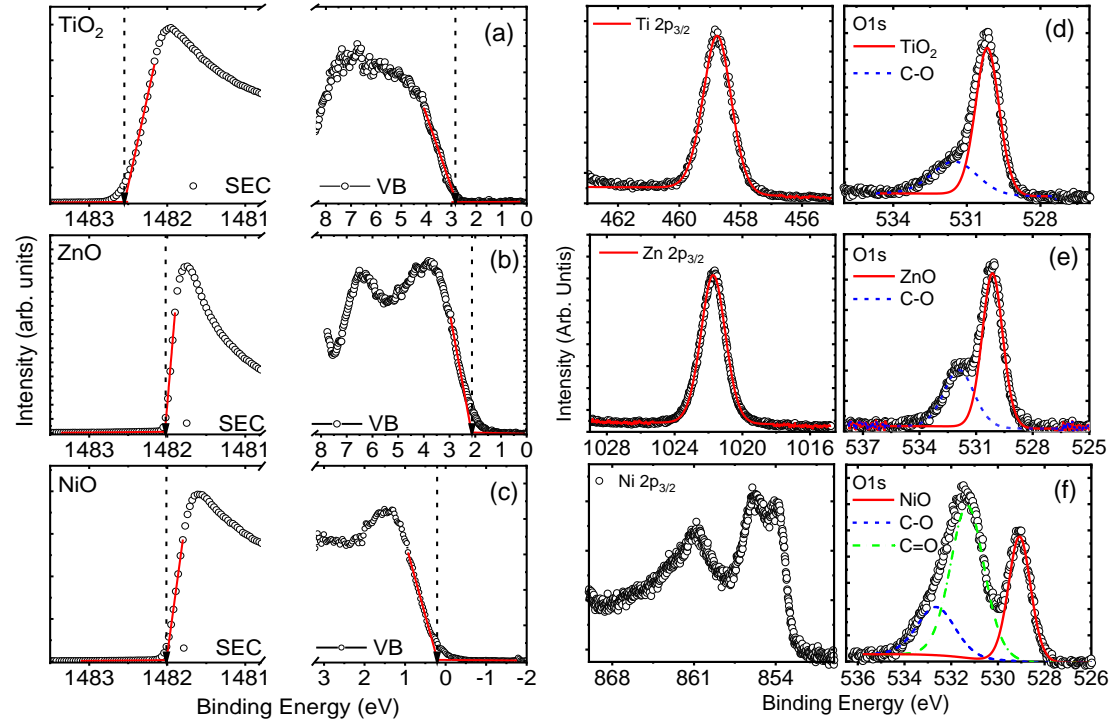


FIG. 3.

This is the author's peer reviewed, accepted manuscript. However, the online version of record will be different from this version once it has been copyedited and typeset.
PLEASE CITE THIS ARTICLE AS DOI: 10.1063/1.50157726

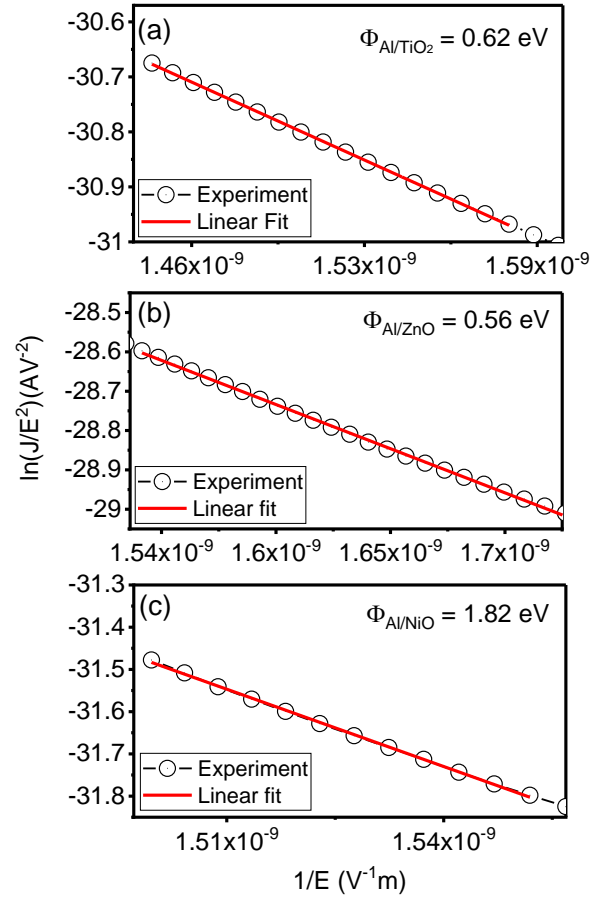


FIG. 4.

This is the author's peer reviewed, accepted manuscript. However, the online version of record will be different from this version once it has been copyedited and typeset.
PLEASE CITE THIS ARTICLE AS DOI: 10.1063/5.0157726

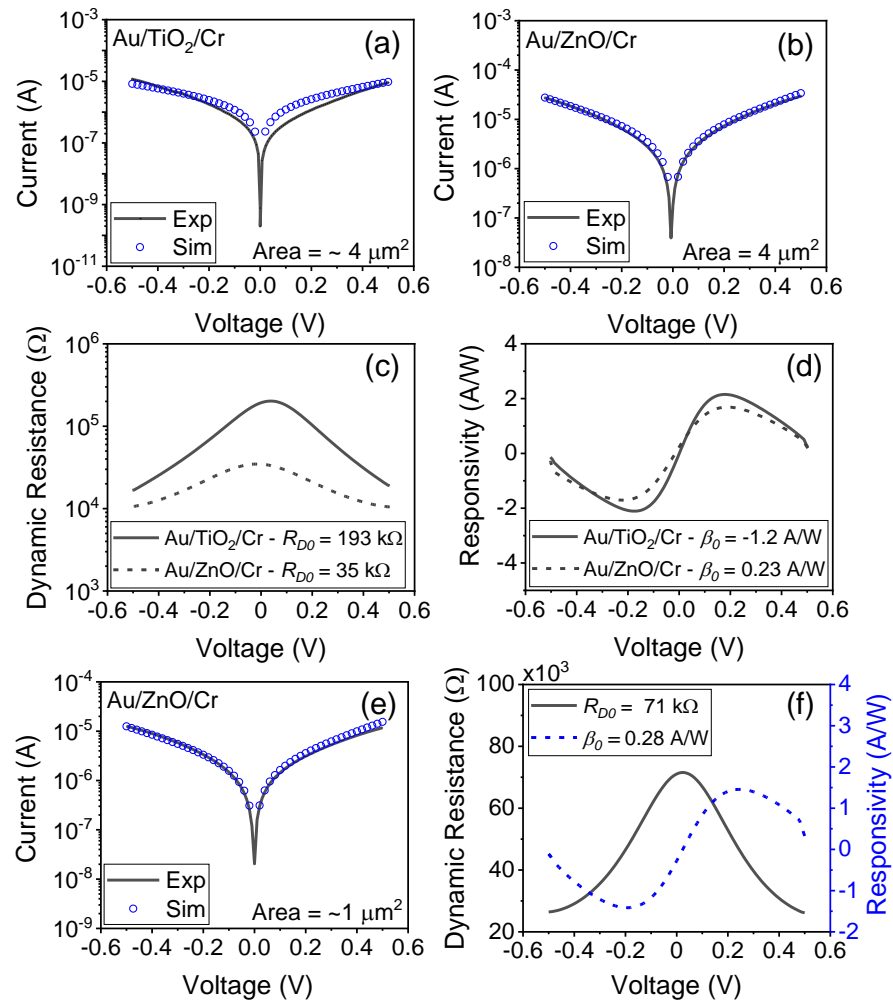


FIG. 5.

This is the author's peer reviewed, accepted manuscript. However, the online version of record will be different from this version once it has been copyedited and typeset.
PLEASE CITE THIS ARTICLE AS DOI: 10.1063/5.0157726

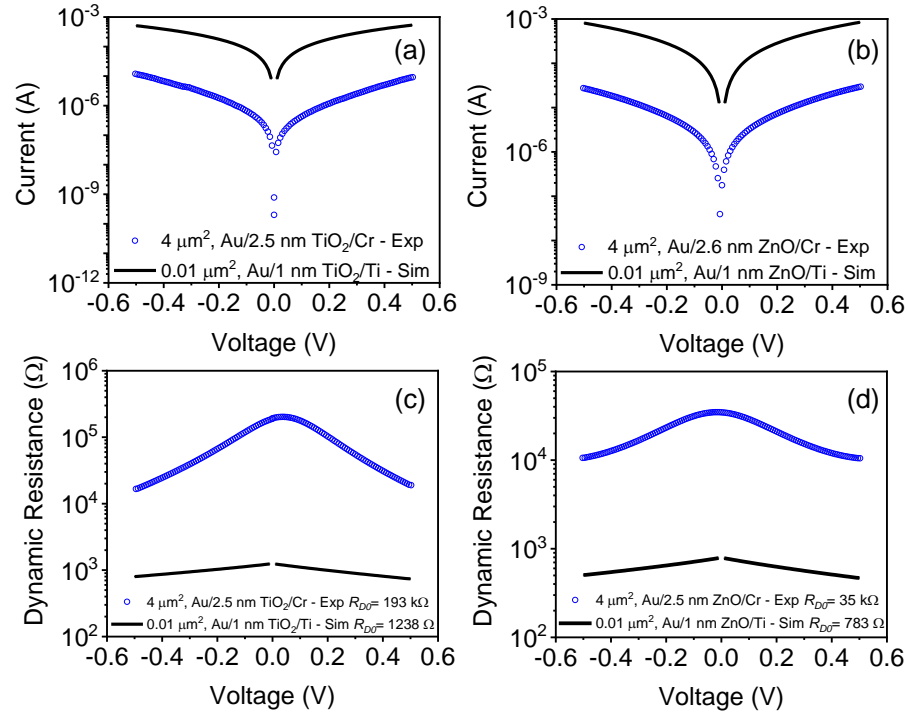


FIG. 6.

This is the author's peer reviewed, accepted manuscript. However, the online version of record will be different from this version once it has been copyedited and typeset.
PLEASE CITE THIS ARTICLE AS DOI: 10.1063/5.0157726

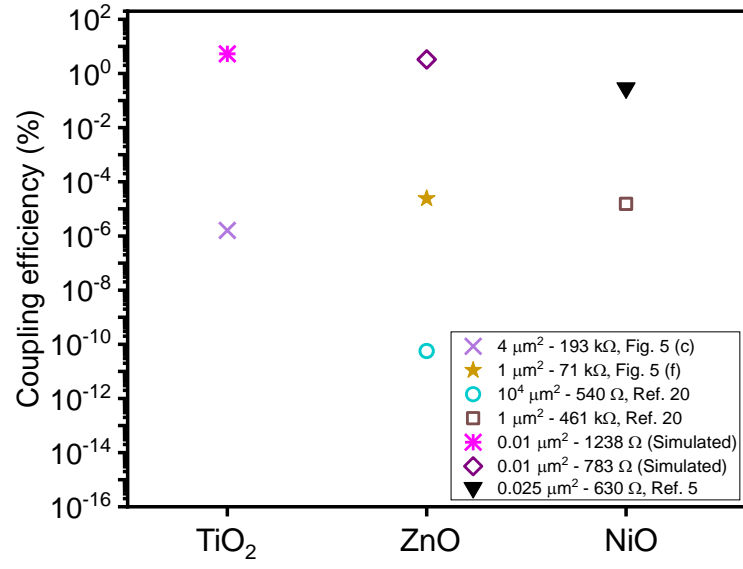


FIG. 7.

This is the author's peer reviewed, accepted manuscript. However, the online version of record will be different from this version once it has been copyedited and typeset.
PLEASE CITE THIS ARTICLE AS DOI: 10.1063/5.0157726

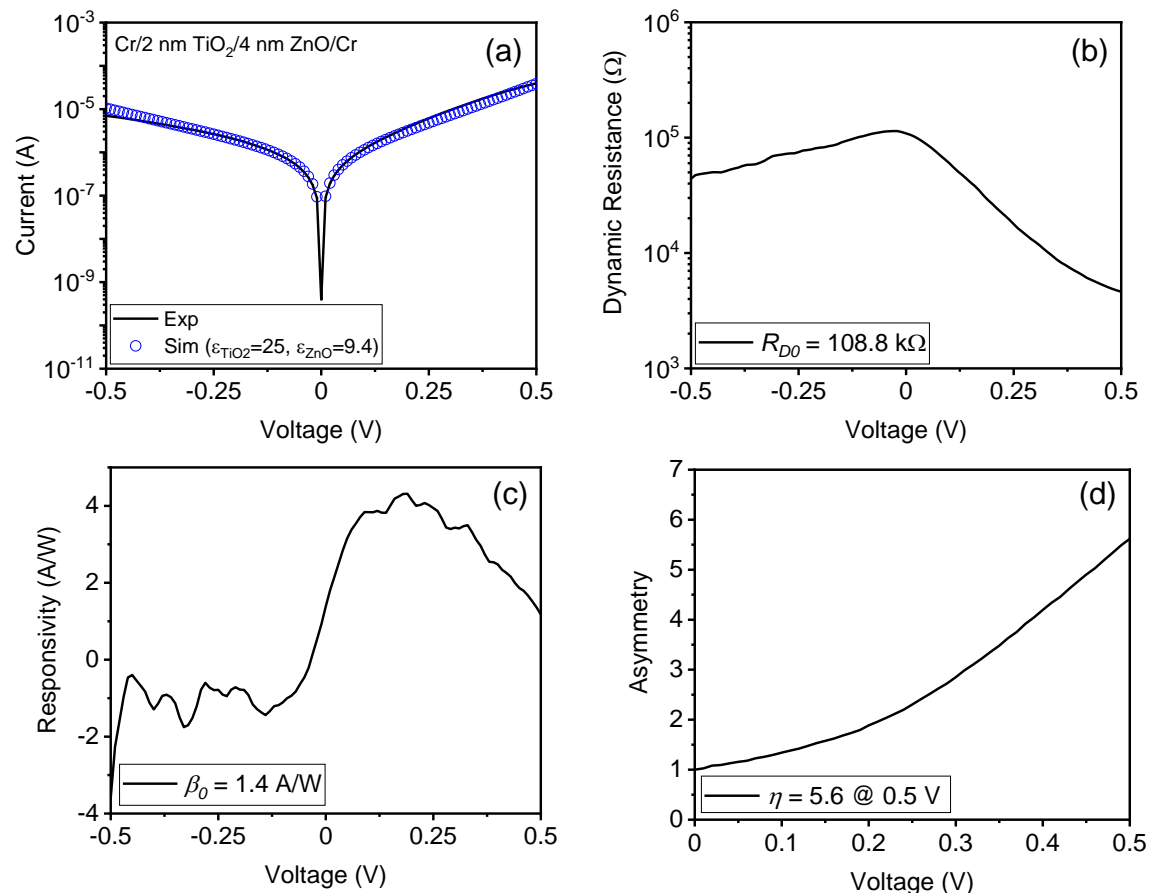
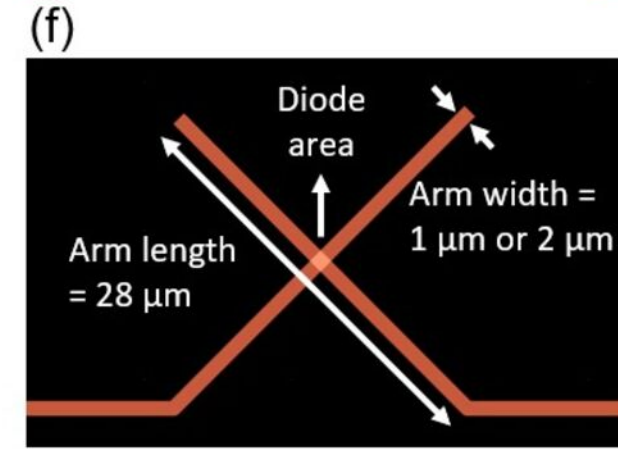
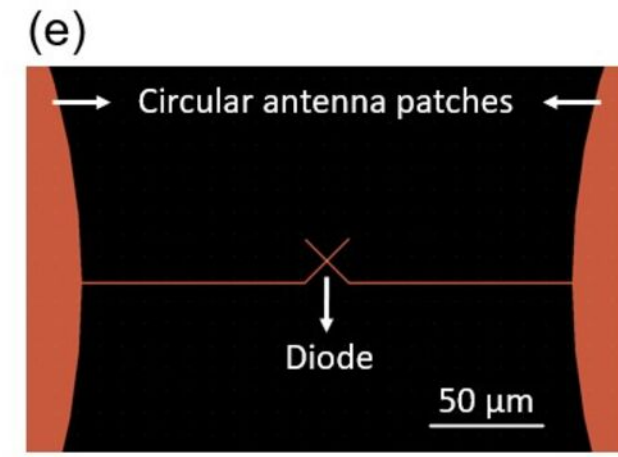
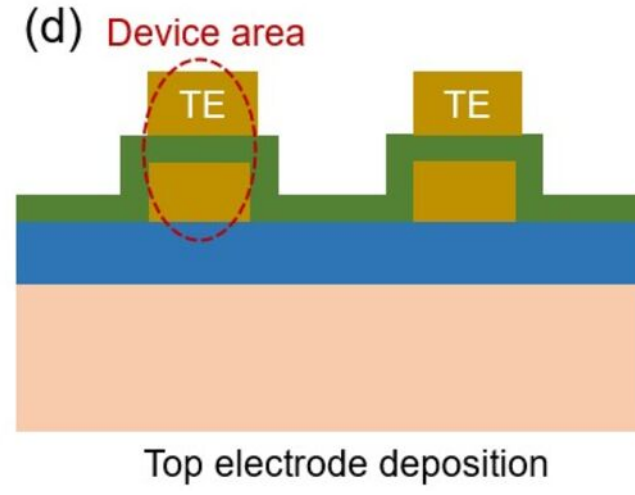
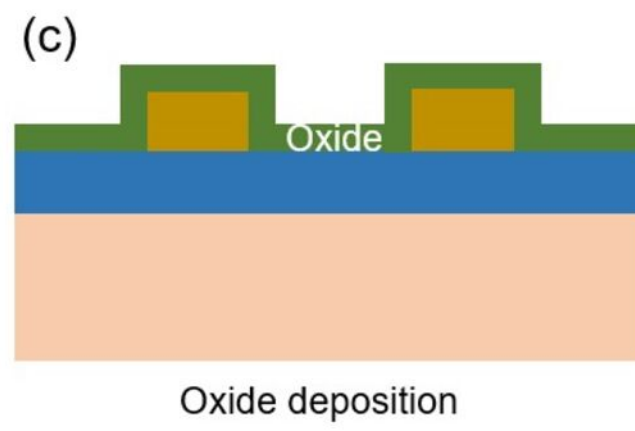
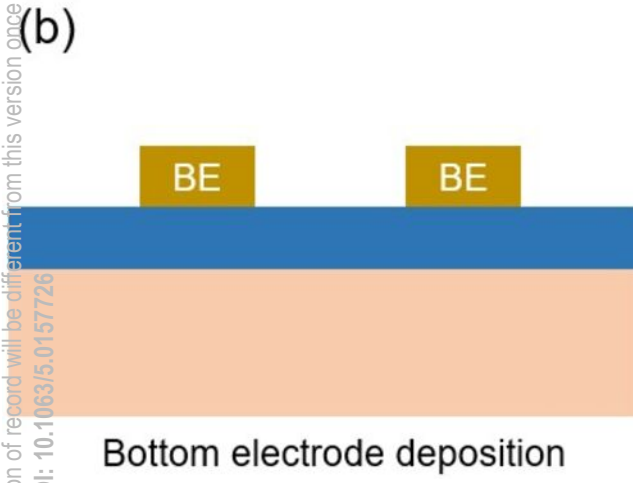
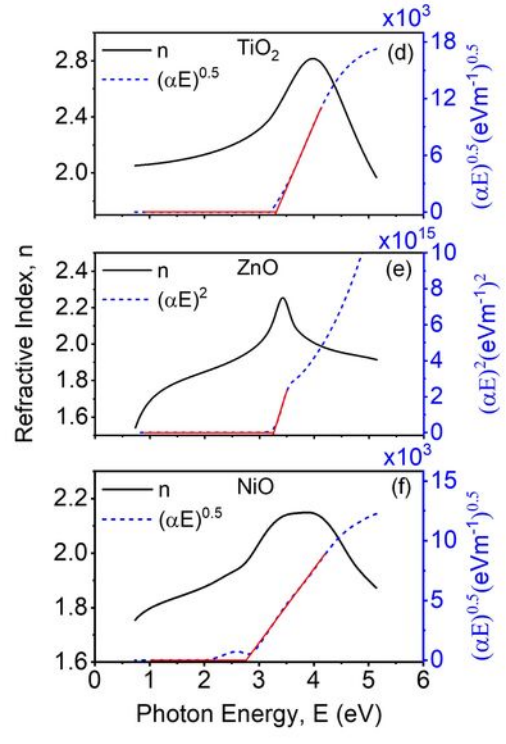
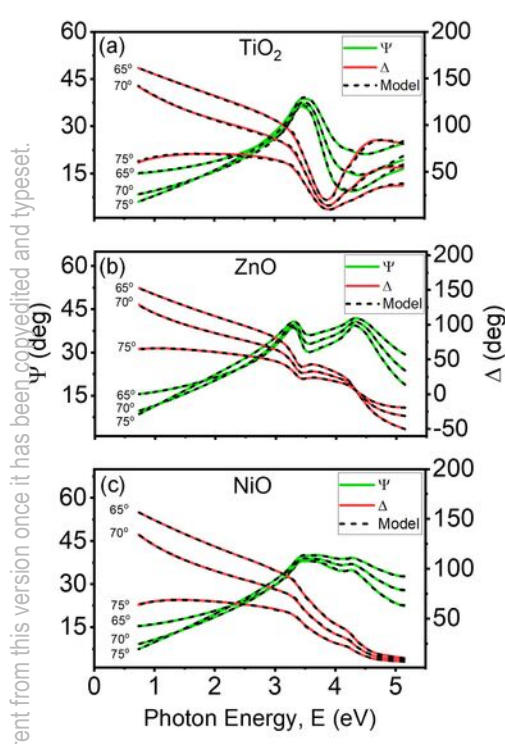


FIG. 8.

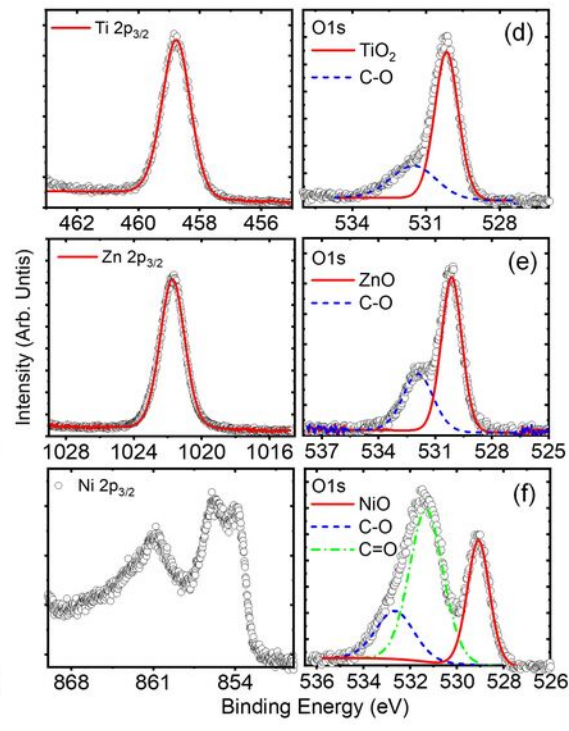
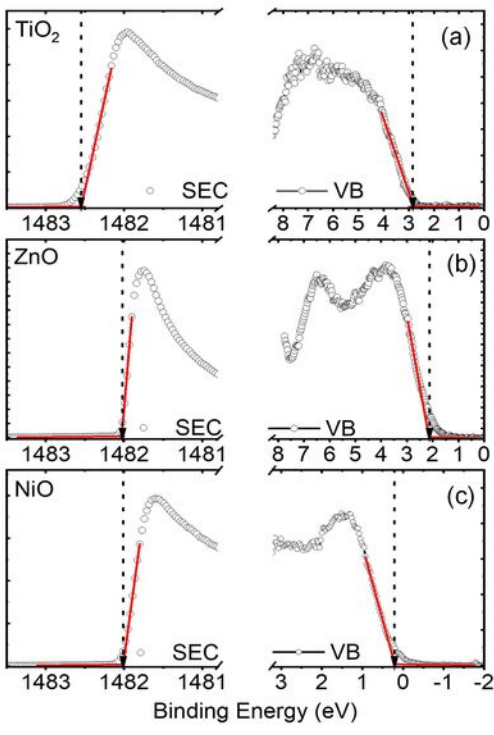
This is the author's peer reviewed, accepted manuscript. However, the online version of record will be different from this version once it has been copyedited and typeset.
PLEASE CITE THIS ARTICLE AS DOI: 10.1063/5.0157726



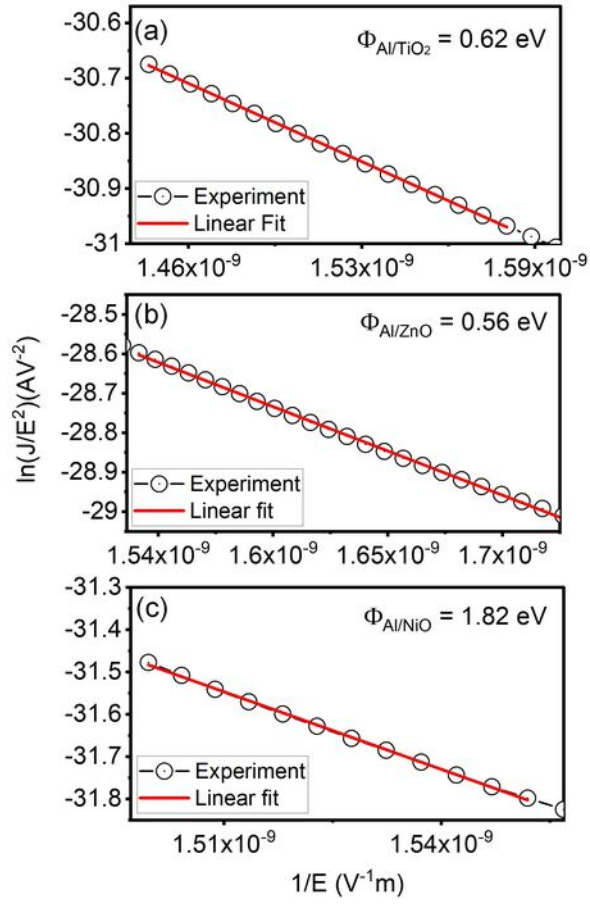
This is the author's peer reviewed, accepted manuscript. However, the online version of record will be different from this version once it has been copyedited and typeset.
PLEASE CITE THIS ARTICLE AS DOI: 10.1063/5.0157726



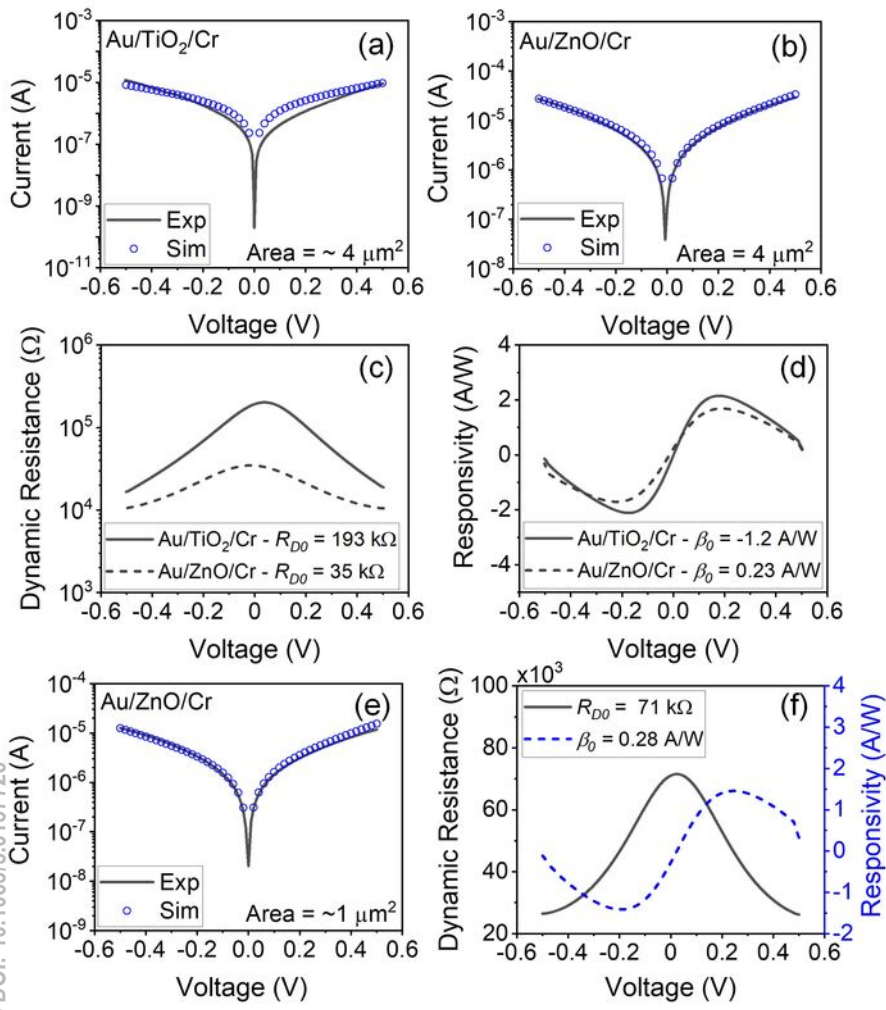
This is the author's peer reviewed, accepted manuscript. However, the online version of record will be different from this version once it has been fully proofread and typeset.
PLEASE CITE THIS ARTICLE AS DOI: 10.1063/5.0157726



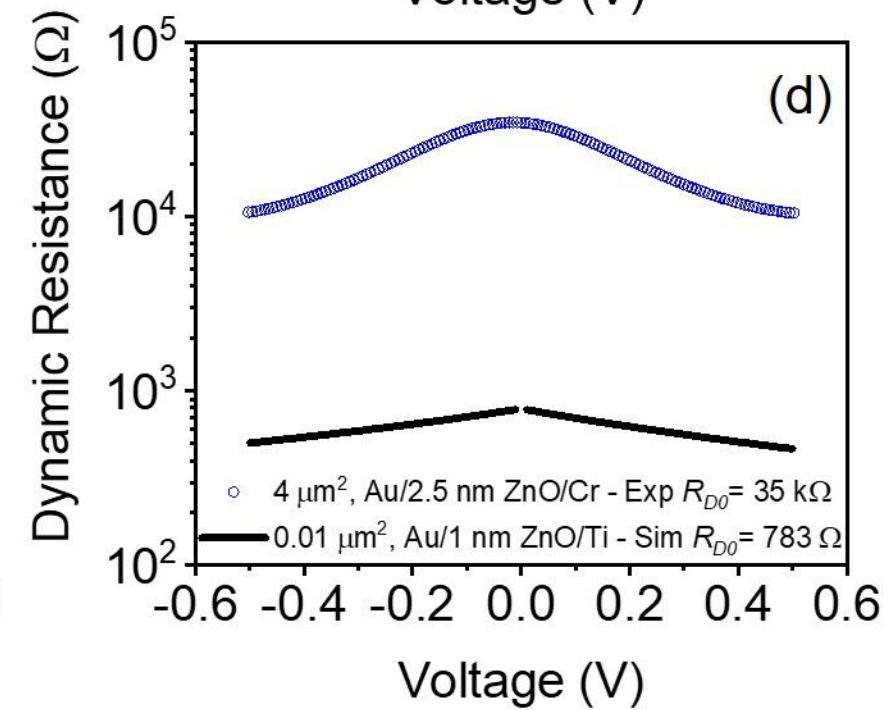
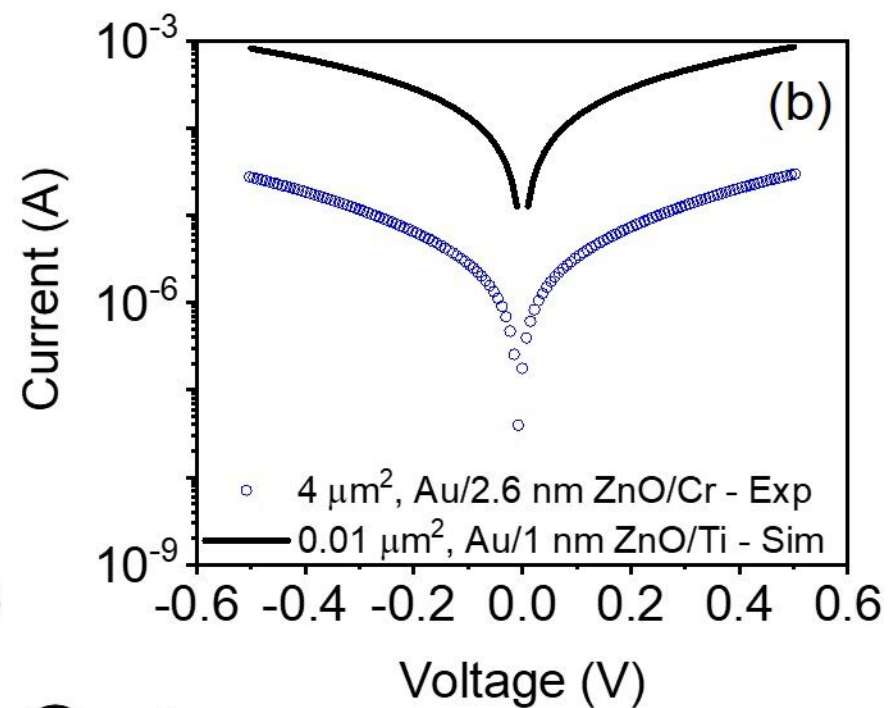
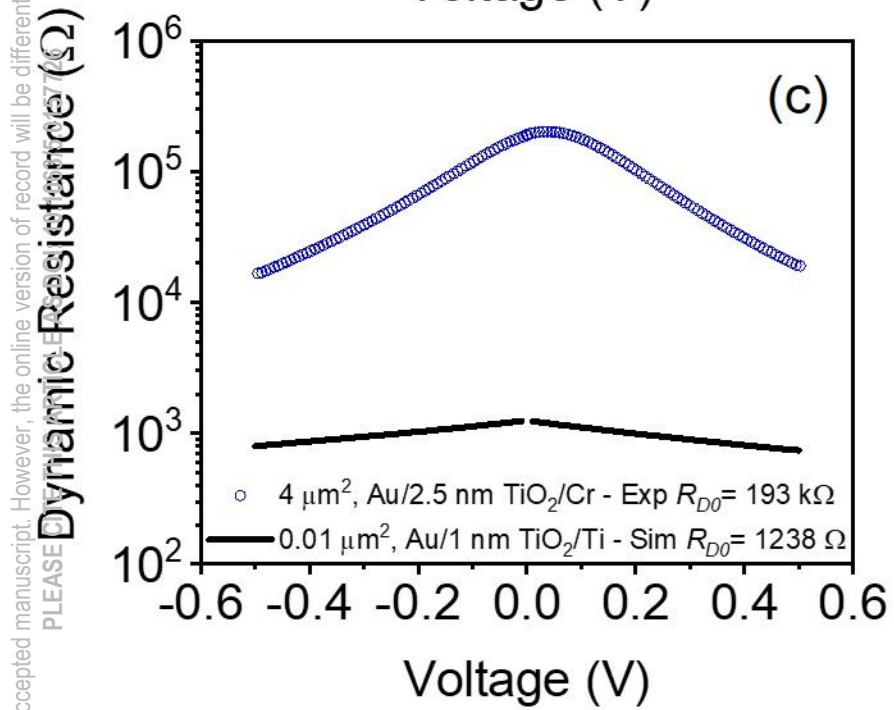
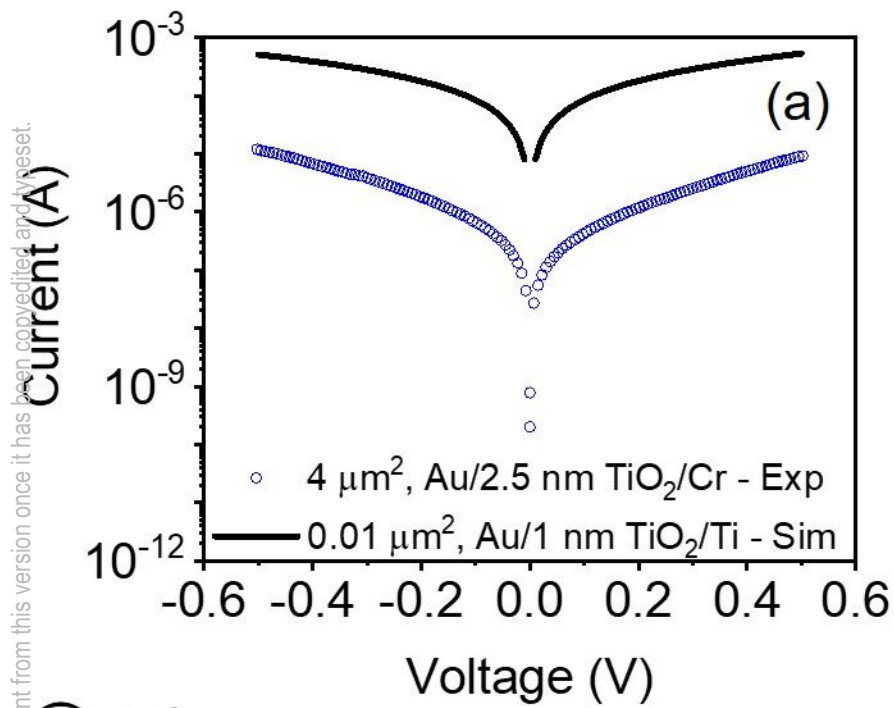
This is the author's peer reviewed, accepted manuscript. However, the online version of record will be different from this version once it has been copyedited and typeset.
PLEASE CITE THIS ARTICLE AS DOI: 10.1063/5.0157726



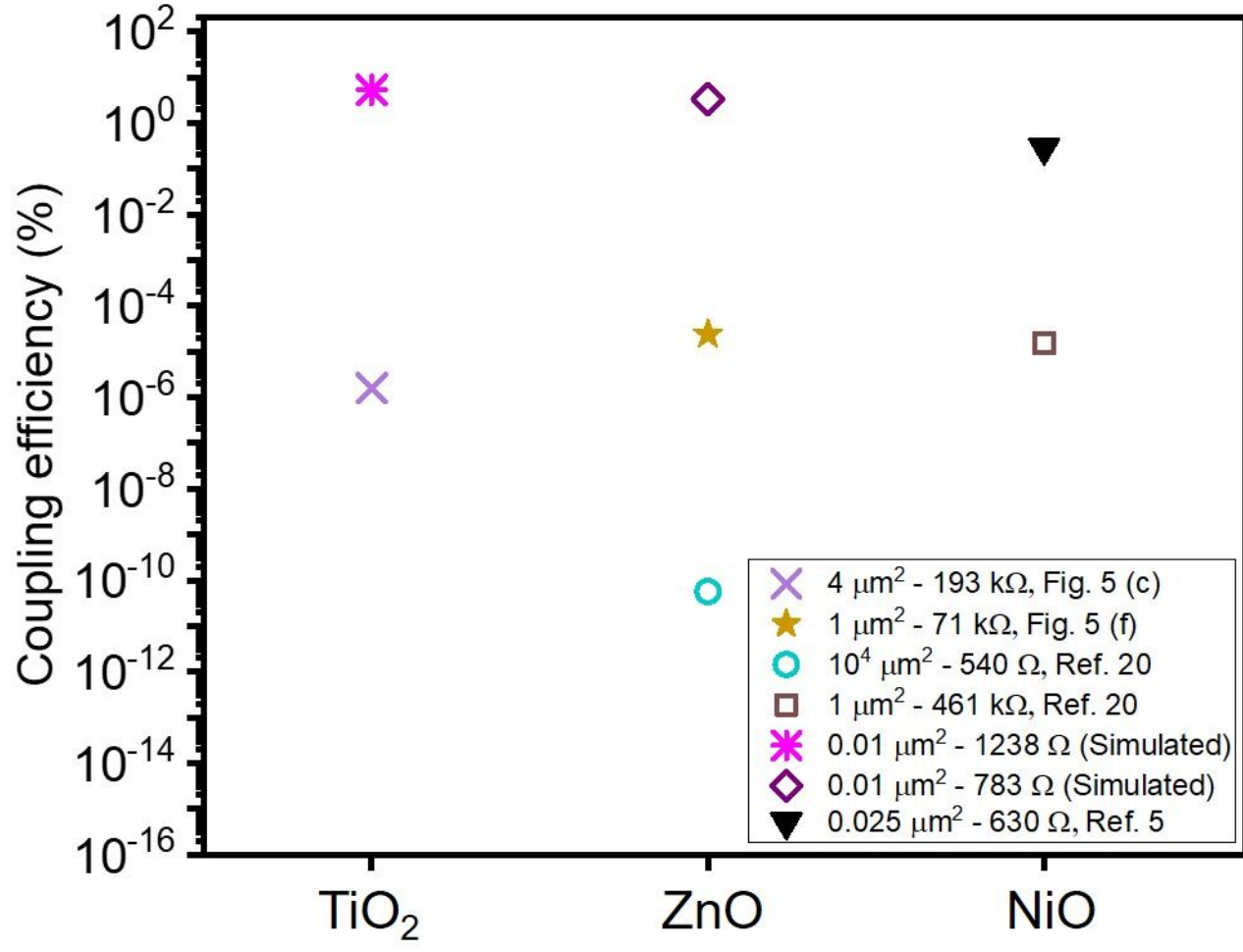
This is the author's peer reviewed, accepted manuscript. However, the online version of record will be different from this version once it has been copyedited and typeset.
PLEASE CITE THIS ARTICLE AS DOI: 10.1063/5.0157726

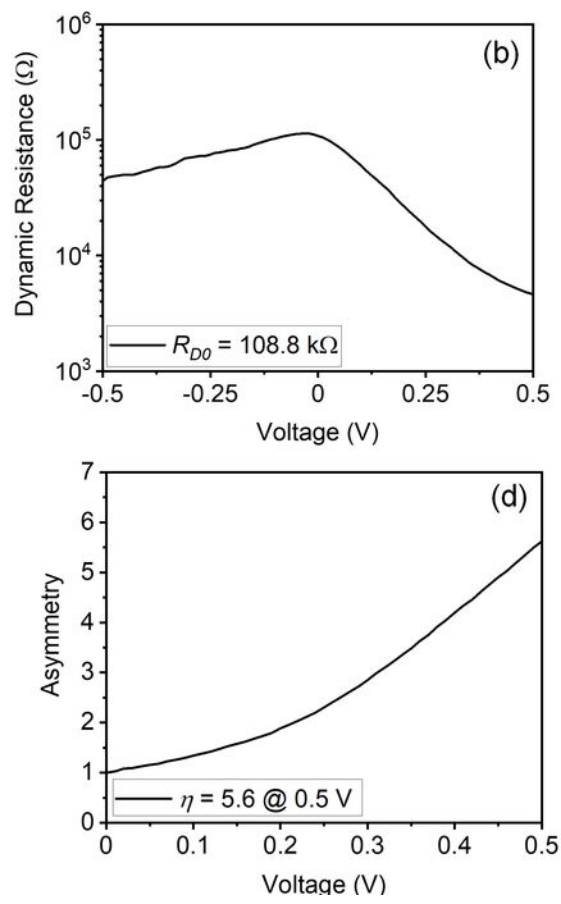
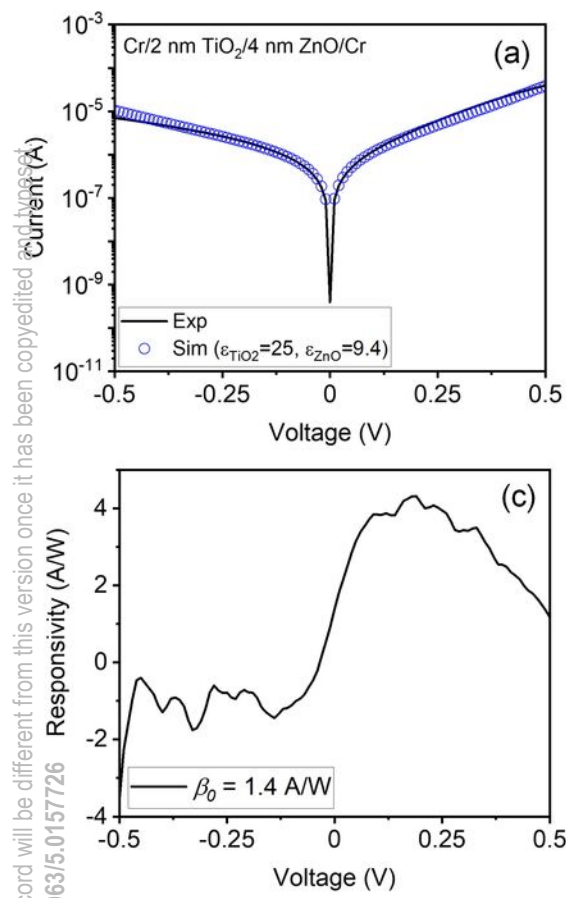


This is the author's peer reviewed, accepted manuscript. However, the online version of record will be different from this version once it has been copyedited and typeset. PLEASE DO NOT DISTRIBUTE OR REPRODUCE THIS MANUSCRIPT WITHOUT THE PERMISSION OF THE AMERICAN PHYSICAL SOCIETY.



This is the author's peer reviewed, accepted manuscript. However, the online version of record will be different from this version once it has been copyedited and typeset.
PLEASE CITE THIS ARTICLE AS DOI: 10.1063/5.0157726





This is the author's peer reviewed, accepted manuscript. However, the online version of record will be different from this version once it has been copyedited and typeset.
PLEASE CITE THIS ARTICLE AS DOI: 10.1063/5.0157726